Atacama Cosmology Telescope: The persistence of neutrino self-interaction in cosmological measurements

Christina D. Kreisch,[1] Minsu Park,[2] Erminia Calabrese,[3] Francis-Yan Cyr-Racine,[4] Rui An,[5] J. Richard Bond,[6] Olivier Doré,[7,8] Jo Dunkley,[9,1] Patricio Gallardo,[10] Vera Gluscevic,[5] J. Colin Hill,[11,12] Adam D. Hincks,[13,14] Mathew S. Madhavacheril,[15] Jeff McMahon,[16,10,17,18] Kavilan Moodley,[19,20] Thomas W. Morris,[9] Federico Nati,[21] Lyman A. Page,[9] Bruce Partridge,[22] Maria Salatino,[23,24] Cristóbal Sifón,[25] David N. Spergel,[12,1] Cristian Vargas,[26] and Edward J. Wollack[27]

[1]Department of Astrophysical Sciences, Princeton University, Princeton, New Jersey 08544, USA
[2]Center for Particle Cosmology, Department of Physics and Astronomy, University of Pennsylvania, Philadelphia, Pennsylvania 19104, USA
[3]School of Physics and Astronomy, Cardiff University, The Parade, Cardiff CF24 3AA, United Kingdom
[4]Department of Physics and Astronomy, University of New Mexico, 210 Yale Blvd NE, Albuquerque, New Mexico 87106, USA
[5]Department of Physics and Astronomy, University of Southern California, Los Angeles, California 90007, USA
[6]Canadian Institute for Theoretical Astrophysics, University of Toronto, 60 St. George St., Toronto, Ontario M5S 3H8, Canada
[7]Jet Propulsion Laboratory, California Institute of Technology, Pasadena, California 91109, USA
[8]California Institute of Technology, Pasadena, California 91125, USA
[9]Joseph Henry Laboratories of Physics, Jadwin Hall, Princeton University, Princeton, New Jersey 08544, USA
[10]Kavli Institute for Cosmological Physics, University of Chicago, Chicago, Illinois 60637, USA
[11]Department of Physics, Columbia University, New York, New York 10027, USA
[12]Center for Computational Astrophysics, Flatiron Institute, New York, New York 10010, USA
[13]David A. Dunlap Department of Astronomy and Astrophysics, University of Toronto, 50 St. George St., Toronto, Ontario M5S 3H4, Canada
[14]Specola Vaticana (Vatican Observatory), V-00120 Vatican City State
[15]Perimeter Institute for Theoretical Physics, 31 Caroline Street N, Waterloo Ontario N2L 2Y5, Canada
[16]Department of Astronomy and Astrophysics, University of Chicago, Chicago, Illinois 60637, USA
[17]Department of Physics, University of Chicago, Chicago, Illinois 60637, USA
[18]Enrico Fermi Institute, University of Chicago, Chicago, Illinois 60637, USA
[19]Astrophysics Research Centre, University of KwaZulu-Natal, Westville Campus, Durban 4041, South Africa
[20]School of Mathematics, Statistics and Computer Science, University of KwaZulu-Natal, Westville Campus, Durban 4041, South Africa
[21]Department of Physics, University of Milano-Bicocca, Piazza della Scienza 3, 20126 Milano, Italy
[22]Department of Astronomy, Haverford College, Haverford, Pennsylvania 19041, USA
[23]Stanford University, Stanford, California 94305, USA
[24]Kavli Institute for Particle Astrophysics and Cosmology, Stanford, California 94305, USA
[25]Instituto de Física, Pontificia Universidad Católica de Valparaíso, Casilla 4059, Valparaíso, Chile
[26]Instituto de Astrofísica and Centro de Astro-Ingeniería, Facultad de Física, Pontificia Universidad Católica de Chile, Av. Vicuña Mackenna 4860, 7820436 Macul, Santiago, Chile
[27]NASA Goddard Space Flight Center, 8800 Greenbelt Rd, Greenbelt, Maryland 20771, USA

We use data from the Atacama Cosmology Telescope (ACT) DR4 to search for the presence of neutrino self-interaction in the cosmic microwave background. Consistent with prior works, the posterior distributions we find are bimodal, with one mode consistent with ΛCDM and one where neutrinos strongly self-interact. By combining ACT data with large-scale information from *WMAP*, we find that a delayed onset of neutrino free streaming caused by significantly strong neutrino self-interaction is compatible with these data at the $2 - 3\sigma$ level. As seen in the past, the preference shifts to ΛCDM with the inclusion of *Planck* data. We determine that the preference for strong neutrino self-interaction is largely driven by angular scales corresponding to $700 \lesssim \ell \lesssim 1000$ in the ACT E-mode polarization data.

This region is expected to be key to discriminate between neutrino self-interacting modes and will soon be probed with more sensitive data.

I. INTRODUCTION

Neutrinos remain an elusive component of the Standard Models of particle physics and cosmology. While cosmological measurements have placed some of the strongest constraints on the sum of neutrino masses (see e.g., Refs. [1,2]), we do not yet know the value. The precise mechanism for the generation of such neutrino masses is also still uncertain. Further, the presence of anomalies in terrestrial neutrino experiments [3–9] may indicate, if confirmed, that yet unknown physics exists in the neutrino sector, hence providing a window into physics beyond the Standard Model.

In particular, new physics altering the free-streaming nature of neutrinos in the early Universe has received renewed interest in recent years (see e.g., Refs. [10–48]). In the Standard Model, neutrinos decouple from the primordial plasma and begin to free stream when the universe has cooled to a temperature of ∼1.5 MeV. While freely streaming, neutrinos still interact gravitationally with the rest of the Universe, tugging on any particles in their paths while they pass by. Observationally, this damps the amplitude of photon fluctuations and shifts them to slightly larger scales [49–51], impacting the amplitude and phase of the observed cosmic microwave background (CMB) temperature and polarization power spectra.

Introducing new physics in the neutrino sector by allowing them to self-interact can, however, significantly delay the time at which neutrinos begin to free-stream. Such a delay abates how long neutrinos gravitationally tug on the photons, leaving a measurable imprint on the CMB [52,53]. The delay in free-streaming also impacts the evolution of the two Newtonian gravitational potentials ϕ and ψ, leading to scale-dependent effects on the growth of matter fluctuations. See Ref. [54] for a thorough discussion of these effects. Through the combination of effects, neutrino self-interactions can be constrained with CMB measurements, baryon acoustic oscillation (BAO) measurements, and other large-scale structure (LSS) measurements (see e.g., Refs. [13,33,34,44,52,54–58]).

In its simplest implementation, self-interactions can be described by an effective four-fermion interaction parametrized by a dimensionful Fermi-like constant $G_{\rm eff}$ [59]. This effective coupling constant determines the neutrino self-interaction rate, $\Gamma_\nu \propto G_{\rm eff}^2 T_\nu^5$ where T_ν is the homogeneous temperature of the neutrino bath. Since this interaction only happens between neutrinos, it does not alter the physics and timing of neutrinos decoupling from the rest of the primordial plasma, as discussed in Ref. [60].

We note however that any ultraviolet completion of the effective four-fermion interaction is subject to several strong constraints, including from supernovae [61–74], big bang nucleosynthesis [75–77], neutrino observations with the IceCube experiment [59,78,79], particle colliders [80–84], and those arising from meson, leptons, tritium, and gauge-boson decay kinematics [83–88]. Taken literally, these bounds exclude values of $G_{\rm eff}$ large enough to affect cosmological observables. Therefore, the $G_{\rm eff}$ parametrization used in this work should not be interpreted as an actual particle model of neutrino self-interaction, but rather as a proxy controlling the onset of neutrino free-streaming in our Universe.

With this in mind, previous works [13,33–35,44,52,54–58] have interestingly found that an effective neutrino self-interaction strength orders of magnitude larger than the standard electroweak interaction can be compatible with CMB and BAO data. Unlike other popular cosmological extensions, the $G_{\rm eff}$ posterior probability distribution is characterized by two distinct islands in parameter space; a strongly interacting mode, SIν, with $G_{\rm eff} \sim 10^{-1.5}$ MeV^{-2}, and a moderately interacting mode, MIν, with $G_{\rm eff} \sim 10^{-4}$ MeV^{-2} that is nearly indistinguishable from ΛCDM. This bimodality stems from a multiparameter degeneracy with $G_{\rm eff}$ [56] involving the angular size of the baryon-photon sound horizon at last scattering θ_*, the amplitude of scalar fluctuations $A_{\rm s}$, and the scalar spectral index $n_{\rm s}$. The strong neutrino self-interactions of the SIν mode shift the phase and boost the amplitude of the multipoles entering the causal horizon before the onset of neutrino free-streaming. To reconcile these effects with cosmological data, larger θ_* and lower $n_{\rm s}$ values are preferred when $G_{\rm eff}$ is large, which in turns result in a lower value of $A_{\rm s}$ to ensure consistency with low CMB multipoles. On the other hand, the MIν mode is characterized by values of θ_*, $A_{\rm s}$, and $n_{\rm s}$ approximately equal to their ΛCDM values.

The recent special interest for this model arises from the fact that the SIν mode belongs to the family of scenarios that bring the CMB and Cepheid-calibrated SNIa measurements of the Hubble constant, H_0, closer by introducing a new species relevant in the early universe to reduce the sound horizon at recombination (see e.g., Refs. [89,90]). Preferring a higher value of $N_{\rm eff}$, the SIν mode is coincident with larger values of H_0 and lower values of σ_8, the amplitude of linear density fluctuations at $8\ h^{-1}$ Mpc, offering a potential simultaneous resolution to both the σ_8 tension and discrepancies in H_0.

Nevertheless, as discussed in Refs. [33–35,44,54], the inclusion of the *Planck* CMB polarization data [1] disfavors

the SIν mode compared to the MIν, casting serious doubt on the viability of this mechanism to resolve the current tensions (see Ref. [91] for a more detailed explanation of this limitation). Despite being statistically suppressed, the SIν mode is not entirely ruled out by these analyses. This then asks the question of what kind of cosmological data *could* eliminate the viability of a late onset of neutrino free streaming.

The low value of the spectral index n_s associated with the SIν mode provides an important clue: cosmological data probing a broad range of scales can provide an important lever arm to constrain the spectral tilt and detect any deviation from its ΛCDM value. High-resolution observations of the CMB temperature and polarization spectra probing small angular scales inaccessible to the *Planck* satellite are a promising candidate for such an observational constraint. Changes to neutrino free-streaming also leave a distinct fingerprint via a phase shift in the angular peak position θ_s. Thus, discriminating polarization measurements can offer another window into constraining neutrino interactions [92]. In this work, we use high-resolution CMB data from four observing seasons of the Atacama Cosmology Telescope (ACT) [93] to probe neutrino self-interaction in the early universe, which is a step towards higher sensitivity measurements from the complete ACT dataset, the Simons Observatory [94] and CMB-S4 [95].

Previous works have shown the compatibility of ACT measurements with other models increasing the sound horizon at recombination, such as early dark energy (EDE) and pseudoscalar sterile neutrino self-interactions [96,97]. Though the physics of how they increase the inferred H_0 from the CMB is similar, the underlying physics and the subsequent perturbation theory and phenomenology can be vastly different, thus motivating further exploration of these class of models with a wide variety of future datasets.

We show below that a delayed onset of neutrino free streaming brought on by significant neutrino self interactions still appears compatible with CMB observations at small angular scales from ACT. This is the case for both ACT alone and in combination with data from the Wilkinson Microwave Anisotropy Probe (*WMAP*) [98,99].

The paper is organized as follows. In Sec. II, we present the cosmological models, data, parameter choices, and statistical tools used in our analyses. Our main results are presented in Sec. III. In Sec. IV we highlight the importance of the ACT E-mode polarization for our results. We consider the impact of BAO measurements on our results in Sec. V and briefly discuss our systematic tests in Sec. VI. We conclude in Sec. VII.

II. DATA AND METHODOLOGY

A. Models, data, and parameter choices

Our baseline cosmological model includes three massive neutrinos with degenerate masses that can scatter among themselves with an interaction rate $\Gamma_\nu \propto G_{\mathrm{eff}}^2 T_\nu^5$. This parallels the analysis done by *Planck* [1].[1] The details of the Boltzmann equations involving such massive self-interacting neutrinos are provided in Ref. [54] (see also Ref. [100]). Within this baseline model, the parameters N_{eff} (which is used to adjust the neutrino temperature T_ν) and the sum of neutrino masses $\sum m_\nu$ are also allowed to vary freely from their standard values of 3.046 eV and 0.06 eV respectively. Our baseline model is thus described by a total of nine parameters once the six standard ΛCDM parameters[2] are included. This model is denoted as "$G_{\mathrm{eff}} + N_{\mathrm{eff}} + \sum m_\nu$" in what follows. We also consider a simpler extension of ΛCDM in which only the neutrino interaction strength G_{eff} is added, with N_{eff} and $\sum m_\nu$ fixed at their standard values. In this case, we adopt the standard practice of considering a single neutrino mass eigenstate carrying all the mass. This model is simply referred to as "G_{eff}".

Throughout our analysis, we used modified versions of the codes CAMB[3] [101] and CosmoMC+Multinest [102,103], equivalent to those used in Ref. [54]. This analysis framework assumes a linear evolution of perturbations. Although negligible at the scales probed by *Planck*, at smaller scales like those measured by ACT, nonlinear gravitational lensing effects impact Σm_ν and N_{eff} estimates and therefore it is likely that they will also alter estimates of G_{eff}. However, we will show later that, despite entering the nonlinear regime for lensing, multipoles above 2500 contribute negligible information to the constraint and therefore a linear analysis here is valid. For future analyses with even stronger influence from $\ell > 2500$, analyzing neutrino self-interactions in the non-linear regime may become necessary.

We use uniform priors on all parameters, except for the *Planck* absolute map-level calibration parameter by the square which all *Planck* spectra are divided which has the Gaussian prior $y_{\mathrm{cal}} = 1.0000 \pm 0.0025$, and the optical depth to reionization which has the Gaussian prior $\tau = 0.065 \pm 0.015$ (see Ref. [93]) and replaces low-ℓ polarization data. As in previous work, we place a uniform prior on the logarithm of the coupling constant G_{eff}, but we here extend the lower range of the prior to -8.0 to include smaller coupling values and allow for any shift in the MIν mode location. (All prior ranges are summarized in Table I.) We also utilize nested sampling [104] to thoroughly sample the multimodal posteriors. For this we use 2000 live points, set the target sampling efficiency to 0.3, set the accuracy threshold on the log Bayesian evidence to 20% to ensure the accuracy of credible intervals. We refer to "modes" as disjoint regions of parameter space that

---

[1]Our analysis here differs from that presented in Ref. [54], which used a single massive neutrinos containing all the mass, in addition to massless neutrinos.

[2]Baryon density $\Omega_b h^2$, cold dark matter density $\Omega_c h^2$, angular peak position θ_s, spectral index n_s and amplitude A_s, and optical depth to reionization τ.

[3]https://github.com/ckreisch/IntNuCAMB.

TABLE I.   Adopted prior ranges.

Parameter	Range
$\log_{10}(G_{\mathrm{eff}}\mathrm{MeV}^2)$	$[-8.0, -0.000001]$[a]
$\sum m_\nu$ [eV]	$[0.0001, 1.5]$
N_{eff}	$[0.0, 5.0]$
$\Omega_b h^2$	$[0.01, 0.04]$
$\Omega_c h^2$	$[0.08, 0.16]$
$100\theta_{\mathrm{MC}}$	$[1.03, 1.05]$
τ	$[0.01, 0.25]$
$\ln(10^{10} A_s)$	$[2, 4]$
n_s	$[0.85, 1.1]$
y_{cal}	$[0.9, 1.1]$
y_p	$[0.9, 1.1]$
A_{SZ}	$[0.0, 2.0]$

[a]The lower bound employed in previous works was -6. Here we take -8 as the lower bound in case higher ℓs are sensitive to extremely small changes in G_{eff}.

isolate the islands of the multimodal posterior distribution. We utilize the mode separation feature in the Multinest algorithm [103] to isolate each mode and compute the parameter posterior distributions for that mode.

In this work we present results on neutrino self-interactions in the presence of the ACT DR4 data. We further combine ACT with *WMAP* and *Planck* CMB data, as well as a selection of low-redshift datasets. We denote the data as follows:

(i) ACT: ACT CMB `actpollite_dr4` likelihood for observing seasons 2013–2016 (DR4), containing TT (temperature autocorrelation) measurements spanning $600 < \ell < 4126$ and TE (temperature-polarization correlation) and EE (polarization-autocorrelation) measurements spanning $350 < \ell < 4126$ [105].

(ii) *Planck*: *Planck* 2018 CMB `plik_lite` high-ℓ likelihood, containing TT measurements spanning $30 < \ell < 2508$ and TE/EE measurements spanning $30 < \ell < 1996$, as well as the `commander` low-ℓ TT likelihood, with measurements spanning $2 < \ell < 29$ [106]. We use the lite high-ℓ likelihood that marginalizes over nuisance parameters to reduce the number of free parameters for its speed and to be consistent with what previous works on this model used.

(iii) *WMAP*: *WMAP* CMB 9-year observations, containing TT measurements spanning $2 < \ell < 1200$ and TE measurements spanning $24 < \ell < 800$ [98,99].

(iv) BAO: Baryon acoustic oscillation (BAO) measurements from Sloan Digital Sky Survey Main Galaxy Sample, Six-degree Field Galaxy Survey, and Data Release 12 [107–109].

(v) Lens: *Planck* CMB lensing data from the 2018 release containing lensing multipoles $8 \leq L \leq 400$ [110]. This is only included when also adding BAO

to combinations with *Planck*. Thus, we do not make note of the lensing measurement when labeling the data combination.

When combining ACT with *Planck* or *WMAP*, we follow the procedure described in Ref. [93], i.e., we remove ACT TT data below $\ell < 1800$ in analyses with *Planck* while we use the full ACT dataset in combination with *WMAP*.

B. Model-comparison tools

We use a variety of techniques to assess the statistical significance of the models we consider. We assess the relative statistical significance between two modes of the posterior by computing their maximum likelihood ratio,

$$\mathcal{R}_{\mathrm{SI}\nu} = \frac{\max\left[\mathcal{L}(\theta_{\mathrm{SI}\nu}|\mathbf{d})\right]}{\max\left[\mathcal{L}(\theta_{\mathrm{MI}\nu}|\mathbf{d})\right]}, \tag{1}$$

where $\theta_{\mathrm{SI}\nu}$ and $\theta_{\mathrm{MI}\nu}$ are the parameters describing the SIν and MIν modes' best-fit parameters, respectively.

To assess how well the different models fit the data, we also compute $\Delta\chi^2$ values. We then translate these values into a significance in terms of Gaussian standard deviations (i.e., σs). We assume that $\Delta\chi^2$ is distributed according to the χ^2-distribution. When comparing fits across different numbers of free parameters, we assume the χ^2-distribution with k degrees of freedom where k is the difference in parameter numbers. This effectively penalizes the additional parameters. Then we find the σ (Gaussian significance) whose C.L. matches the cumulative probability function at the given $\Delta\chi^2$, following the same method as in [96]. We note, however, that the multidimensional posteriors may not be sufficiently Gaussian for either mode (especially MIν), so Gaussian significances should be interpreted with caution.

We finally compute the Akaike information criterion (AIC) [111] to penalize the extra parameters added to the interacting neutrino model. The ΔAIC between two models is computed as

$$\Delta\mathrm{AIC} = \mathrm{AIC}_{\mathrm{I}\nu} - \mathrm{AIC}_{\Lambda\mathrm{CDM}} = \Delta\chi^2 + 2\Delta k. \tag{2}$$

A lower AIC value provides a better fit, so a negative ΔAIC value indicates preference for interacting neutrinos.

To compare different dataset combinations' preference for either mode, we compute the Bayes factor

$$\mathcal{B}_{\mathrm{SI}\nu} \equiv \frac{\mathcal{Z}_{\mathrm{SI}\nu}}{\mathcal{Z}_{\mathrm{MI}\nu}} \tag{3}$$

which compares the modes' Bayesian evidence $\mathcal{Z}$, defined as the parameter-averaged likelihood of the data,

$$\mathcal{Z}_j \equiv \mathrm{Pr}\,(\mathbf{d}|\mathcal{M}_j) = \int_{\Omega_\theta} \mathrm{Pr}\,(\mathbf{d}|\theta, \mathcal{M}_j)\,\mathrm{Pr}\,(\theta|\mathcal{M}_j)d\theta, \tag{4}$$

where **d** is the data, θ are the parameters describing model $\mathcal{M}$, $\mathcal{M}_j$ denotes the jth mode of the posterior distribution on the space of θ, and Ω_θ is the entire parameter space. Note that we are using the Bayes factor to compare the modes' statistical significances, instead of model comparison. [56] We note that $\mathcal{Z}$ is weakly sensitive to the prior volume when the likelihood is uninformative near the prior boundary (which will be the case for the MIν in our analyses). Thus, the exact values of $\mathcal{B}_{\mathrm{SI}\nu}$ we report here have a mild (linear) dependence on our choice of prior distribution. However, even significantly extending our prior distribution on G_{eff} to include the Standard Model Fermi constant value ($G_{\mathrm{eff}} \sim 10^{-11}$ MeV^{-2}) could at most change $\mathcal{B}_{\mathrm{SI}\nu}$ by a factor of order unity, hence not qualitatively changing our conclusions. Moreover, given a choice of prior, the relative values of $\mathcal{B}_{\mathrm{SI}\nu}$ for different dataset combinations are an informative indicator of the corresponding preference for one mode versus the other among these data.

III. CMB-ONLY RESULTS WITH EMPHASIS ON ACT

The parameter constraints on our baseline $G_{\mathrm{eff}} + N_{\mathrm{eff}} + \sum m_\nu$ model using various combinations of ACT, *WMAP*, and *Planck* data are shown in Fig. 1. ACT data, both alone and when combined with *WMAP*, show some preference for strong neutrino self-interactions and the resulting delayed onset of neutrino free streaming. The distribution of G_{eff} is bimodal for all dataset combinations presented, but the
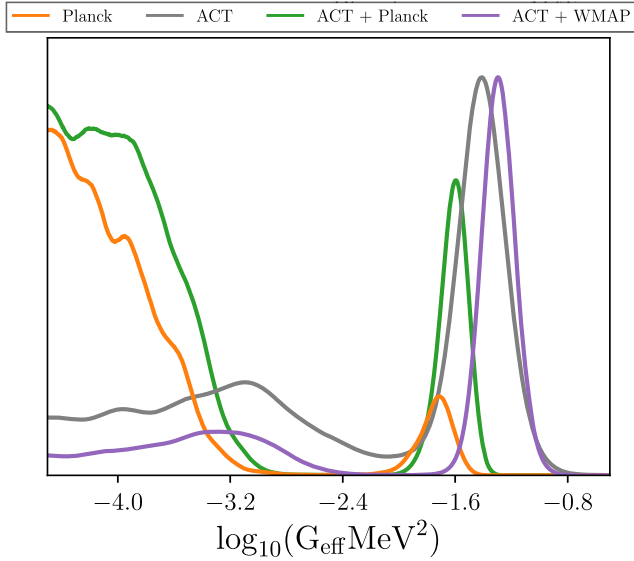

FIG. 1. Marginalized posterior distribution of G_{eff} for the different CMB datasets for our baseline $G_{\mathrm{eff}} + N_{\mathrm{eff}} + \sum m_\nu$ model. We limit the range of the horizontal axis displayed here (despite the prior extending farther in either direction) to better show the details of the two posterior modes. We minimally smooth the posteriors in order to maintain the bimodal features. As such, small values of G_{eff} can appear unconverged, as indicated by the wiggly lines for low G_{eff}.

TABLE II. Mode comparison for our baseline $G_{\mathrm{eff}} + N_{\mathrm{eff}} + \sum m_\nu$ model for different CMB dataset combinations. $\mathcal{B}_{\mathrm{SI}\nu}$ is the Bayes factor between the SIν and the MIν modes, $\mathcal{R}_{\mathrm{SI}\nu}$ is the maximum likelihood ratio, and $\Delta\chi^2_{\mathrm{Tot}} = \chi^2_{\mathrm{SI}\nu} - \chi^2_{\mathrm{MI}\nu}$.

	ACT	*Planck*	ACT + *WMAP*	ACT + *Planck*
$\mathcal{B}_{\mathrm{SI}\nu}$	1.5 ± 0.2	0.01 ± 0.01	2.8 ± 0.6	0.05 ± 0.02
$\mathcal{R}_{\mathrm{SI}\nu}$	2.6	0.4	6.5	1.1
$\Delta\chi^2_{\mathrm{Tot}}$	-1.9	1.8	-3.7	-0.2

strongly interacting mode is relatively preferred with the ACT data alone as well as the ACT data combined with *WMAP* data, whereas the weakly interacting mode, compatible with ΛCDM, is preferred by the *Planck* data. Adding ACT data to *Planck* increases the probability of the SIν mode compared to *Planck* alone, but keeps an overall preference for the MIν mode. It is interesting to note that the ACT + *WMAP* combination, which together probe a broad range of angular scales, comparatively to *Planck* favors a late onset of neutrino free streaming, although ΛCDM still provides a good fit to the data. The improvement in overall χ^2 for this interacting model, compared to ΛCDM, is 13.7 for three extra parameters for ACT + *WMAP*, which we translate to a 2.9σ preference. For ACT + *Planck* the improvement in χ^2 is only 1.7 for the SIν mode, with ΛCDM preferred. The physical reasons driving these preferences and differences will be discussed in the next few sections.

In Table II we quantify the relative significance of the SIν and MIν modes within our baseline model. For ACT-only, we find a Bayes factor of 1.5 ± 0.2.[4] With *WMAP* added, the Bayes factor grows to 2.8 ± 0.6, corresponding to an increased preference for SIν [see Table 4 in Ref. [112] where the inverse corresponds to our definition of the Bayes factor]. *Planck* alone and ACT + *Planck* show values below 1, showing a greater preference for MIν than the other dataset combinations. Similar conclusions can be drawn from the maximum likelihood ratios.

Credible intervals for the different cosmological parameters within our baseline model are given in Appendix A in Table IV for the SIν mode and in Table V for the MIν mode.

We note that our ACT results do not yet have the sensitivity to weigh on the discussions around tensions between the CMB and the local Universe estimates of both

---

[4]We note that Multinest was not able to automatically separate the modes with ACT-only. To compare evidence, we ran two separate chains with a prior on $\log_{10}(G_{\mathrm{eff}}\mathrm{MeV}^2)$ of $[-4.0, -2.0]$ and $[-2.0, 0.0]$, respectively, and with equivalent priors for all other parameters. We chose these G_{eff} priors in order to maintain the same prior volume between the two modes, and we safely are able to cut at -4 instead of -8 since the ACT-only 1D G_{eff} posterior drops off, as in Fig. 1.

the Hubble constant, H_0, and the amplitude of matter clustering, σ_8 (see also Appendix E).[5]

A. The efficacy of G_{eff} alone

To explore how much of the slight preference for the SIν mode we see when ACT is involved is influenced by some movements in other neutrino parameters degenerate with N_{eff}, we test a simplified model in which we fix $N_{\text{eff}} = 3.046$ and $\sum m_\nu = 0.06$ eV, letting only G_{eff} and the standard six ΛCDM parameters vary freely. We find that while removing the N_{eff} and $\sum m_\nu$ freedom has little impact on the SIν mode for ACT + *WMAP*, it does significantly suppress the existence of the MIν mode for this data combination. This indicates that the relevance of the MIν mode depends on the values recovered for other neutrino parameters in the fit, while the existence of the SIν mode is not driven by the specific values of N_{eff} and $\sum m_\nu$. In other words, the delayed onset of neutrino free-streaming caused by a large value of G_{eff} is key to ACT's preference for the SIν mode. Indeed, we find that adding the single G_{eff} parameter improves the fit to ACT data moderately more than other simple extensions considered in the literature or more than the combination $N_{\text{eff}} + \sum m_\nu$ (see Tables VI and VII in Appendix A). Here the G_{eff} model slightly increases H_0 compared to the ΛCDM result, with $H_0 = 69.3 \pm 1.1$ versus 67.6 ± 1.1 km/s/Mpc for ΛCDM [93].

Why does G_{eff} have such an impact on the fit to ACT + *WMAP* data? As a single parameter, it influences the CMB power spectra in three ways; amplitude, phase, and tilt as described in Ref. [54]. This can be seen by looking at the correlation between G_{eff} and the parameters $A_s e^{-2\tau}$, θ_*, and n_s (shown in Fig. 5 in Appendix C). Changing the value of G_{eff} between the two modes of the distribution is, thus, able to accomplish the equivalent of adjusting three parameters. We note, however, that G_{eff}'s impacts on the power spectra are coupled; large G_{eff} causes a boost in amplitude which coincides with a shift towards small scales and a blue tilt (all compared to ΛCDM). With three parameters that can either increase or decrease in values, there are a total of eight different combinations of changes to the power spectra. Remarkably, G_{eff} is able to capture the one combination[6] that is actually favored by the data (discussed more in Sec. IV).

B. The role of $\Omega_b h^2$, N_{eff}, and n_s

The three effects generated by G_{eff} are also able to compensate for other fluctuations seen in the ACT fits.

As discussed in Ref. [93], ACT data alone prefer a $2.3 - 2.7\sigma$ low fluctuation of $\Omega_b h^2$ and high fluctuation of n_s within ΛCDM compared to *WMAP* and *Planck*. The low $\Omega_b h^2$ value damps the first acoustic peak and small angular scales, and also produces a slight phase shift towards larger scales (due to the reduced baryon loading of the primeval plasma). This small-scale damping is then compensated by the high n_s value, which tilts the spectra up. This movement occurs along a strong degeneracy line and is alleviated when large angular scales are added to ACT. Allowing also N_{eff} to vary for ACT data alone yields similarly low $\Omega_b h^2$ values, but with an n_s value more similar to *Planck* accompanied by a low N_{eff} centered at ~ 2.3, disfavoring the larger relativistic degrees of freedom $N_{\text{eff}} = 3.5$ at 4σ, as discussed in Ref. [93]. N_{eff} and n_s are highly degenerate due to large N_{eff} causing small-scale damping [50] and higher n_s being able to undo this damping. While most of the $\Omega_b h^2$–n_s ACT fit can be shifted with *WMAP* data, the low fluctuation in N_{eff} remains (ACT + *WMAP* prefers N_{eff} values $\sim 2.3\sigma$ lower than the standard value) and leaves room for the neutrino strong mode.

Strong neutrino self-interactions, i.e., large values of G_{eff}, are able to undo the damping and phase shift from the low preferred $\Omega_b h^2$ by boosting the spectra and shifting it towards small scales. This is done by exploiting the multiparameter degeneracy between G_{eff}, A_s and n_s described in Ref. [56], which results in lower values of both A_s and n_s as compared to ΛCDM. At the same time, strong neutrino self-interactions allow N_{eff} to be closer to its standard value due to absence of free-streaming phase and amplitude shift [49] on the CMB in this case (see Table IV in Appendix A). Appendix G explores the additional degeneracy with the primordial helium abundance.

TABLE III. Comparison to ΛCDM for the strongly-interacting neutrino mode ($\Delta\chi^2 = \chi^2_{\text{SI}\nu} - \chi^2_{\Lambda\text{CDM}}$) for our baseline model.

Parameter	ACT	*Planck*	ACT + *WMAP*	ACT + *Planck*
$\Delta\chi^2_{\text{ACT}}$	−10.0		−14.9	−5.2
$\Delta\chi^2_{\text{ACT:TT}}$[a]	−2.7		−1.9	−1.1
$\Delta\chi^2_{\text{ACT:TE}}$	0.03		−7.0	−4.3
$\Delta\chi^2_{\text{ACT:EE}}$	−7.3		−6.0	0.2
$\Delta\chi^2_{\text{low}\ell}$		3.1		4.9
$\Delta\chi^2_{\text{high}\ell}$		0.4		2.0
$\Delta\chi^2_{WMAP}$			0.8	
$\Delta\chi^2_{\text{CMB Total}}$	−10.0	3.5	−14.1	1.7
$\Delta\chi^2_{\text{prior}}$	0.09	−3.1	0.4	−3.4
$\Delta\chi^2_{\text{Total}}$	−10.0	0.4	−13.7	−1.7
ΔAIC	−4.0	6.4	−7.7	4.3

[a]Hereinafter, each $\Delta\chi^2_{\text{ACT:X}}$ accounts once for the cross-correlation with the other components of ACT data such that the three $\Delta\chi^2_{\text{ACT:X}}$ add up to $\Delta\chi^2_{\text{ACT}}$ without overcounting.
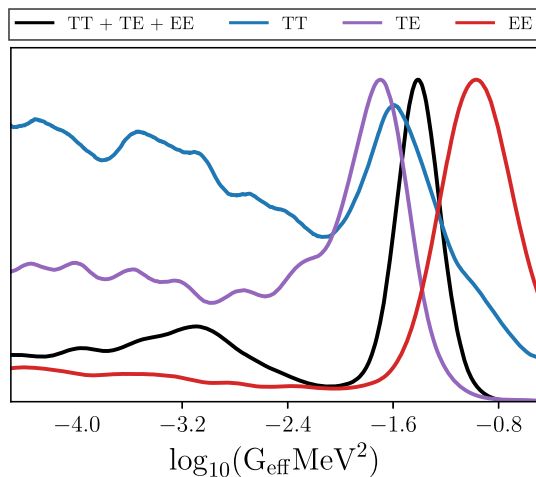
---

[5]From Fig. 5 of Sec. C we also infer that fitting SIν to ACT + *WMAP* does not result in a simultaneous higher H_0 and lower σ_8, as was the case with SIν and *Planck* in previous works. Introducing G_{eff} and N_{eff} does not change the values of H_0 and σ_8 away from the ΛCDM values much. Introducing Σm_ν actually pushes both H_0 and σ_8 *lower*.

[6]It captures only one combination rather than two because when G_{eff} is small, the physics is equivalent to ΛCDM.

FIG. 2. ACT 1D posteriors for G_{eff} in the baseline model for the full TT + TE + EE data and for fits of separate spectra. We note again that we minimally smooth the posteriors, so low values of G_{eff} can appear unconverged.

IV. THE ROLE OF E-MODE POLARIZATION

ACT's preference for a delayed onset of neutrino free streaming is predominantly driven by its E-mode polarization spectrum. We show in Table III the $\Delta\chi^2$ between SIν (nine parameters) and ΛCDM (six parameters) for different CMB data combinations. The largest $\Delta\chi^2$ in favor of the SIν mode occurs for ACT's E-mode polarization data for ACT alone, with $\Delta\chi^2_{ACT:EE} = -7.3$, and ACT + WMAP, with $\Delta\chi^2_{ACT:EE} = -6.0$. In Fig. 2 we show the G_{eff} posterior distribution for the ACT combined dataset and separate constraints from its TT, TE, and EE data.[7] While the TT and TE data show some preference for the SIν mode, ACT's EE data dominates the preference for a delayed onset of neutrino free streaming as the MIν mode nearly disappears in this case.

The addition of *Planck* data neutralizes ACT's E-mode polarization preference. *Planck* polarization data is signal dominated in windows below $\ell \approx 700$ (see Fig. 17 in Ref. [113]), and can therefore statistically overpower ACT's polarization preferences in this multipole range, which, as we will see below, plays a significant role in these constraints. Given that *WMAP* does not include EE data, the inclusion of *WMAP* does not suppress ACT EE data's preference for SIν. Further, this combination also sees a preference for SIν coming from the ACT TE data, with $\Delta\chi^2_{ACT:TE} = -7.0$.

Why does ACT's E-mode polarization prefer a delayed onset of neutrino free streaming while *Planck*'s does not? To answer this question, we show the $-\chi^2$ per degree of freedom ($-\chi^2/$d.o.f.) for the SIν mode, MIν mode, and

---

[7]These were obtained by running separate nested sampling runs with ACT TT data alone, TE data alone, and EE data alone.

ΛCDM as a function of the maximum ℓ used for the TT, TE, EE, and combined ACT data in Fig. 3. We use the ACT + WMAP best-fit models and we indicate with a dashed line a reference value of $-\chi^2/$d.o.f. $= -1$.

Overall, both the SIν and MIν modes provide a better fit than ΛCDM to the ACT E-mode polarization data (see Appendix B for tables comparing the MIν mode to ΛCDM). Both modes have larger $-\chi^2/$d.o.f. than ΛCDM in the bottom right panel of Fig. 3, which focuses on the E-mode polarization. For the range $700 \lesssim \ell \lesssim 1000$ in this panel, as ℓ_{max} increases the SIν mode rapidly provides a better fit to the data than either the MIν mode or ΛCDM. The MIν mode fits the TE cross-correlation data better than the SIν mode in the same range, but the margin between the modes is twice as large with the EE autocorrelation. *Ultimately the effect in the $700 \lesssim \ell \lesssim 1000$ range of the E-mode polarization drives the total likelihood in favor of the SIν mode.* Beyond $\ell \sim 1000$, there is not significant information added by smaller scales to further differentiate the two interacting neutrino modes. Finally, angular scales corresponding to $\ell \gtrsim 1700$ do not incorporate additional information to further improve the fit of ΛCDM over the 2 modes. More specifically, we find that removing ACT data at $\ell > 2500$ does not significantly change the posterior distribution on G_{eff}. By contrast, keeping only data at $\ell > 1000$ entirely removes the modest preference for $G_{eff} \sim 10^{-1.6}$ MeV^{-2} and leaves a nearly flat posterior, reinforcing the fact that the preference for the SIν mode is driven by larger angular scales.

Our findings mirror those in Refs. [96,97] showing that the most pertinent feature for the respective extensions to ΛCDM is in the $\ell \lesssim 1000$ range of the EE spectrum of ACT data. This is also in agreement with the theoretical expectation provided in Ref. [114], which concludes that CMB experiments are most sensitive to neutrino interactions at $\ell \lesssim 1000$.

Having identified this important range of angular scales in the E-mode polarization spectrum, we now study the residuals between the best-fit *Planck* ΛCDM cosmological model and the three leading datasets of ACT, *Planck*, and SPT-3G [115] E-mode polarization data in this range. As shown in Fig. 4, residuals for all experiments show a slight upward fluctuation in the range $700 \lesssim \ell \lesssim 1000$, with ACT showing the largest shift. A delayed onset of neutrino free streaming can better capture this upward fluctuation, driving the preference for the SIν mode in the ACT data. Indeed, as described in Ref. [56], Fourier modes corresponding to this particular ℓ range enter the causal horizon close to the onset of neutrino free streaming for the SIν mode, allowing them to be significantly influenced by the modified evolution of the gravitational potentials. The figure also clarifies why the preference is reduced when including *Planck* data: while consistent with both ACT and SPT-3G in this multipole range, *Planck* does not possess such a strong E-mode upward fluctuation.
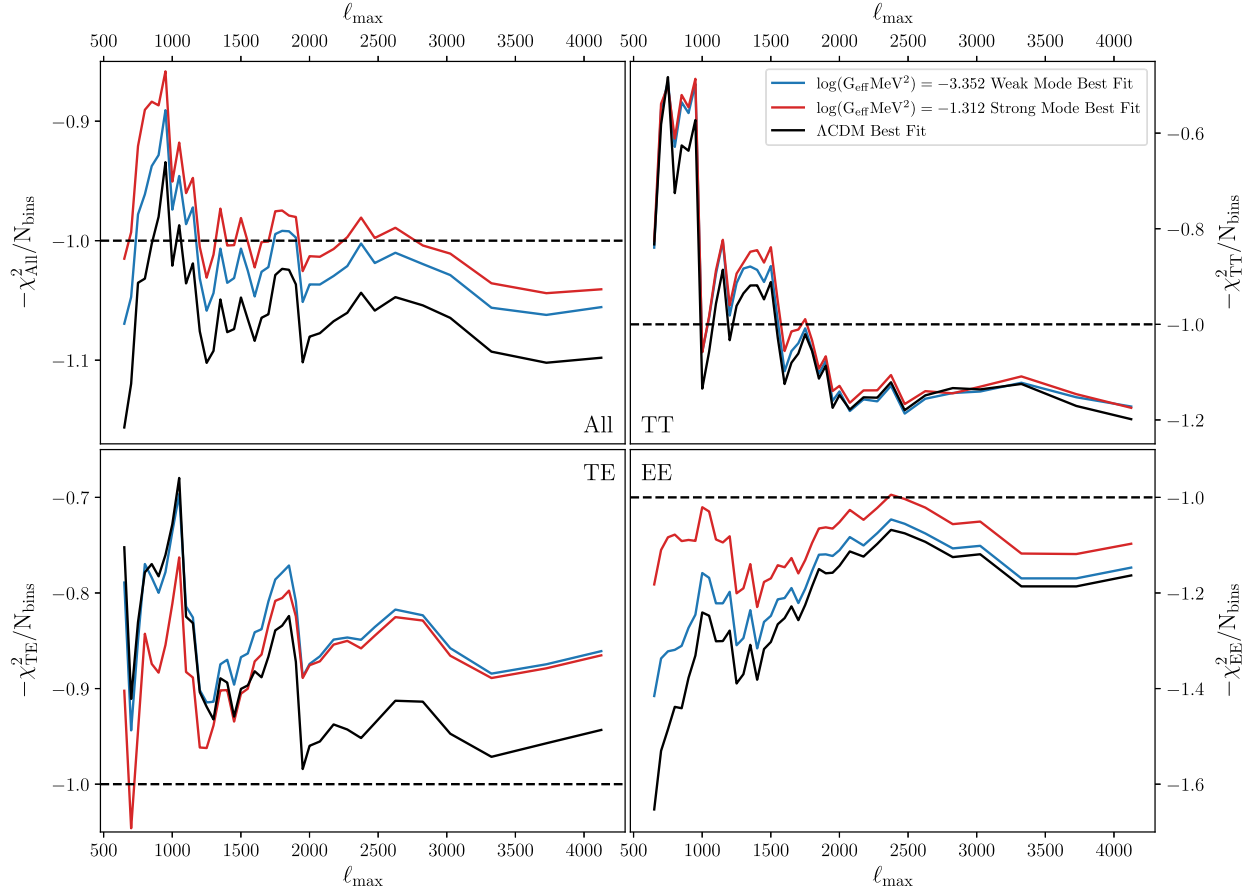
FIG. 3. $-\chi^2/N_{bins}$ as a function of ℓ_{max} where the former is the negative reduced χ^2 and the latter the maximum ℓ used in the likelihood, shown for SIν (in red), MIν (in blue), and ΛCDM (in black) best fits to ACT + *WMAP* data. This is shown for the combined ACT data in top left, TT only in top right, TE only in bottom left, and EE only in bottom right. Overall, it is clear that for most choices of ℓ_{max}, SIν has the largest $-\chi^2/N_{bins}$ across all sectors of ACT data. The top left figure shows the greatest difference between SIν and MIν in the $700 \lesssim \ell \lesssim 1000$ range, which is echoed only by the bottom right, indicating the importance of E-mode polarization in that ℓ range in promoting the favorability of SIν.
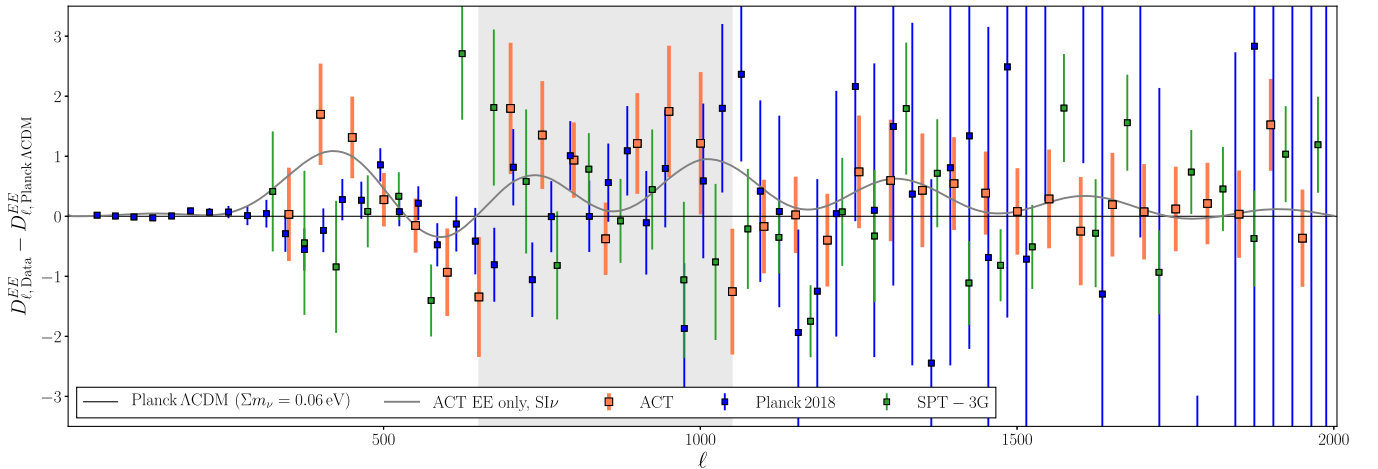
FIG. 4. Residuals of E-mode polarization data for ACT (orange), *Planck* (blue), and SPT-3G (green) data relative to *Planck*'s best-fit ΛCDM model. We overlay the best-fit for SIν for just ACT E-mode polarization in gray (best-fit further described in Sec. IV), and the gray band highlights the multipoles that drive ACT's preference for SIν. Each bin spans 50 multipoles. Note the upwards deviation from the best fit in the $700 \lesssim \ell \lesssim 1000$ range of the ACT and SPT-3G data. The residuals of TT, TE, and EE power spectrum for the full ℓ range are presented in Appendix D.

V. CMB + LENSING + BAO RESULTS

We now expand our analysis beyond CMB-only results and as previously mentioned incorporate BAO and *Planck* CMB lensing data. Overall we find that adding BAO measurements increases the significance of the SIν compared to the MIν mode.[8] Such preference is not surprising for the ACT + *WMAP* CMB dataset; the values of our baseline model's parameters most relevant to BAO (i.e. H_0, Ω_m, and N_{eff}) for ACT + *WMAP* within the SIν mode are closer to their concordance ΛCDM values than those within the MIν mode and therefore BAO further consolidates this preference. We find that the SIν mode has a $\Delta\chi^2 = -13.2$ compared to ΛCDM for ACT + *WMAP* once BAO is included (Table X in Appendix B), roughly corresponding to a 2.9σ preference for a delayed onset of neutrino free streaming. ΛCDM continues to be preferred when adding BAO to ACT + *Planck*.

VI. ROBUSTNESS TESTS

We test the robustness of our results—and in particular the contribution to them from ACT—by examining different partitions of the ACT data independently, and revisiting some of the analysis assumptions:

(i) Figure 2 shows that different spectra (TT, TE, EE) in ACT give very consistent results.

(ii) ACT data are further composed of "deep" maps, spanning 20–340 deg^2, and "wide" maps, spanning 210–1400 deg^2 (see Refs. [93,105]). Both sets contain TT, TE, and EE power spectra spanning the full-ℓ ranges detailed in Sec. II. After constraining the interaction with each set separately, we conclude that the two patches give consistent results but the wide data prefer the SIν mode more than the deep data does. This weaker significance in the deep data is not unexpected, however, as the wide data has smaller errors at large scales, and therefore stronger constraining power, than the deep data at scales that are relevant for this model (See Appendix F for further discussion).

(iii) The difference in mode preference between ACT and *Planck* could also point to a different behavior at large and small scales since the two experiments' constraining power peaks in different regimes [93]. Even if ACT on its own does not yet allow for a high signal-to-noise comparison of the two regimes we run a few tests to check any effect on the results.

We find that the G_{eff} 1D posteriors when we vary the full nine parameter space with all of ACT, or ACT small scales ($\ell > 2500$) removed, or ACT large scales ($\ell < 1000$) removed are all consistent. As mentioned before, for constraints of neutrino self-interaction with ACT data, the critical information is in the large scales and small scales hardly contribute to the demonstrated preference for SIν. This also supports the framework of a linear analysis.

(iv) Finally, we note that multiplying or dividing the ACT TE power spectra by an artificial calibration factor of 1.05 to account for some unknown amplitude offset as in Ref. [93] does not substantially change the results.

VII. CONCLUSIONS

We have shown that ACT DR4 data, both alone and when combined with *WMAP*, display a slight preference for a delayed onset of neutrino free streaming due to neutrino self interactions at the 2–3σ level. Like in previous analyses using CMB data, we find the parameter posteriors to be bimodal. When using ACT the strongly interacting mode representing the delayed onset of neutrino free streaming has a higher likelihood than the ΛCDM analogous, weakly interacting mode. The preference reverts towards ΛCDM when *Planck* data is added to ACT, with the strongly-interacting mode suppressed and the bimodality moving more in favor of the ΛCDM analog model as seen in previous works. We determined that ACT data's preference is primarily driven by angular scale corresponding to $700 \lesssim \ell \lesssim 1000$ in the ACT E-mode polarization data. The impact of *Planck* in the joint fit is mostly due to a wider range of cosmological information provided by *Planck* and in particular in this EE range.

In summary, despite the high-resolution observations of the CMB temperature and polarization spectra we find the posterior to be persistently bimodal and the preference between the modes to be dependent on choice of model (G_{eff} only or $G_{eff} + N_{eff} + \Sigma m_\nu$) and dataset combination. This indicates that we need more data to make any decisive judgements on this model, and motivates searches for unaccounted-for systematic effects in the $500 \lesssim \ell \lesssim 1000$ region in polarization that we highlighted (see also Refs. [96,97]). Alternative new-physics models could also be examined, including those where only a fraction of the neutrinos can self-interact (see e.g., Refs. [33–35]). Our results also call for detailed scrutiny of upcoming ACT polarization data, especially in the $\ell \lesssim 1000$ region.

---

[8]A slight preference for the SIν mode when including BAO and distance ladder H_0 measurements had been noted in Ref. [54], but their analysis only includes *Planck* temperature data. We see that ACT + *WMAP* data when combined with BAO measurements, as well as when combined with local H_0 measurements from SH_0ES, have some preference for late neutrino free streaming. See Appendix E for an updated discussion on neutrino free streaming and local H_0 measurements in light of ACT data.

APPENDIX A: PARAMETER VALUES

In this appendix, we list the credible intervals for the different model parameters used in our analyses. In Table IV, we give the mean parameter values and their 1σ error bars for the SIν mode for four data combinations. The corresponding MIν values are given in Table V.

TABLE IV. Credible intervals (68%) for the SIν mode for our baseline model.

Parameter	ACT	*Planck*	ACT + *WMAP*	ACT + *Planck*
$\Omega_b h^2$	0.02100 ± 0.00050	0.02240 ± 0.00023	0.02188 ± 0.00035	$0.02214^{+0.00024}_{-0.00022}$
$\Omega_c h^2$	$0.1164^{+0.0069}_{-0.0079}$	$0.1165^{+0.0025}_{-0.0036}$	0.1195 ± 0.0053	0.1171 ± 0.0031
$100\theta_{MC}$	1.04709 ± 0.00090	$1.04564^{+0.00054}_{-0.00062}$	1.04757 ± 0.00077	1.04615 ± 0.00046
τ	0.065 ± 0.014	$0.0736^{+0.012}_{-0.0067}$	$0.060^{+0.011}_{-0.012}$	$0.071^{+0.012}_{-0.010}$
$\sum m_\nu$ [eV]	$0.83^{+0.60}_{-0.28}$	$0.106^{+0.029}_{-0.11}$	0.59 ± 0.30	$0.246^{+0.080}_{-0.24}$
N_{eff}	$2.45^{+0.40}_{-0.55}$	$2.79^{+0.16}_{-0.21}$	$2.82^{+0.28}_{-0.33}$	$2.74^{+0.17}_{-0.20}$
$\log_{10}(G_{eff}\mathrm{MeV}^2)$	$-1.42^{+0.19}_{-0.16}$	$-1.73^{+0.13}_{-0.17}$	-1.29 ± 0.11	$-1.61^{+0.11}_{-0.077}$
$\ln(10^{10}A_s)$	2.983 ± 0.032	$3.015^{+0.025}_{-0.015}$	2.976 ± 0.027	$3.010^{+0.026}_{-0.021}$
n_s	$0.913^{+0.027}_{-0.040}$	$0.9312^{+0.0079}_{-0.0070}$	0.921 ± 0.013	0.9267 ± 0.0078
H_0 [km/s/Mpc]	$56.5^{+3.5}_{-7.1}$	66.7 ± 1.9	$62.3^{+3.3}_{-4.7}$	$64.7^{+3.1}_{-2.1}$
Ω_m	$0.471^{+0.10}_{-0.089}$	$0.315^{+0.010}_{-0.017}$	$0.385^{+0.050}_{-0.059}$	$0.341^{+0.015}_{-0.039}$
σ_8	$0.670^{+0.042}_{-0.094}$	$0.817^{+0.028}_{-0.011}$	$0.704^{+0.046}_{-0.072}$	$0.785^{+0.055}_{-0.022}$
Y_P	$0.2361^{+0.0066}_{-0.0077}$	$0.2418^{+0.0024}_{-0.0030}$	0.2420 ± 0.0043	0.2410 ± 0.0027
r_* [Mpc]	149.2 ± 4.7	$146.7^{+2.2}_{-1.6}$	145.9 ± 3.0	146.9 ± 1.9

TABLE V. Credible intervals (68%) for the MIν mode for our baseline model.

Parameter	ACT	*Planck*	ACT + *WMAP*	ACT + *Planck*
$\Omega_b h^2$	$0.02064^{+0.00040}_{-0.00045}$	0.02229 ± 0.00023	$0.02153^{+0.00030}_{-0.00035}$	0.02200 ± 0.00021
$\Omega_c h^2$	$0.1092^{+0.0053}_{-0.0063}$	0.1186 ± 0.0029	$0.1119^{+0.0044}_{-0.0051}$	0.1155 ± 0.0025
$100\theta_{MC}$	$1.04341^{+0.00099}_{-0.0011}$	1.04105 ± 0.00044	1.04255 ± 0.00082	1.04153 ± 0.00039
τ	0.065 ± 0.013	$0.0749^{+0.014}_{-0.0099}$	$0.060^{+0.011}_{-0.012}$	$0.071^{+0.013}_{-0.010}$

(Table continued)

TABLE V. *(Continued)*

Parameter	ACT	*Planck*	ACT + *WMAP*	ACT + *Planck*
$\sum m_\nu$ [eV]	< 0.771	$0.112^{+0.028}_{-0.11}$	$0.70^{+0.30}_{-0.26}$	$0.171^{+0.050}_{-0.17}$
N_{eff}	$2.03^{+0.28}_{-0.42}$	2.95 ± 0.19	$2.37^{+0.25}_{-0.28}$	2.71 ± 0.16
$\log_{10}(G_{\text{eff}}\text{MeV}^2)$	$-3.13^{+0.45}_{-0.62}$	$-5.89^{+0.99}_{-1.8}$	$-4.9^{+2.2}_{-2.5}$	-5.7 ± 1.3
$\ln(10^{10}A_{\text{s}})$	3.019 ± 0.035	$3.081^{+0.029}_{-0.022}$	3.029 ± 0.028	$3.069^{+0.027}_{-0.023}$
n_{s}	$0.905^{+0.024}_{-0.038}$	0.9616 ± 0.0087	0.933 ± 0.014	0.9523 ± 0.0082
H_0 [km/s/Mpc]	$52.0^{+2.4}_{-5.2}$	$66.3^{+2.0}_{-1.5}$	$56.9^{+2.4}_{-3.8}$	$63.9^{+2.4}_{-1.5}$
Ω_{m}	$0.529^{+0.10}_{-0.075}$	$0.323^{+0.010}_{-0.020}$	0.440 ± 0.055	$0.342^{+0.012}_{-0.029}$
σ_8	$0.631^{+0.030}_{-0.076}$	$0.813^{+0.029}_{-0.014}$	$0.665^{+0.036}_{-0.062}$	$0.790^{+0.041}_{-0.017}$
Y_{P}	$0.2297^{+0.0050}_{-0.0064}$	0.2441 ± 0.0026	0.2354 ± 0.0041	0.2405 ± 0.0023
r_* [Mpc]	$153.7^{+4.1}_{-3.6}$	145.3 ± 1.8	150.6 ± 3.0	147.7 ± 1.6

TABLE VI. Credible intervals (68%) for the SIν mode for our simple G_{eff} model.

Parameter	ACT	ACT + *WMAP*	ACT + *Planck*
$\Omega_{\text{b}}h^2$	0.02155 ± 0.00031	0.02222 ± 0.00019	0.02246 ± 0.00014
$\Omega_{\text{c}}h^2$	0.1209 ± 0.0041	0.1211 ± 0.0026	0.1214 ± 0.0013
$100\theta_{\text{MC}}$	$1.0462^{+0.0026}_{-0.0042}$	1.04793 ± 0.00071	$1.04639^{+0.00045}_{-0.00038}$
τ	0.063 ± 0.013	$0.059^{+0.010}_{-0.012}$	$0.0695^{+0.012}_{-0.0084}$
$\log_{10}(G_{\text{eff}}\text{MeV}^2)$	$-2.3^{+1.5}_{-1.1}$	-1.277 ± 0.090	-1.552 ± 0.081
$\ln(10^{10}A_{\text{s}})$	$3.000^{+0.031}_{-0.051}$	2.975 ± 0.021	$3.011^{+0.023}_{-0.018}$
n_{s}	$0.969^{+0.018}_{-0.031}$	0.9334 ± 0.0060	$0.9375^{+0.0050}_{-0.0043}$
H_0 [km/s/Mpc]	68.2 ± 1.6	69.3 ± 1.1	68.84 ± 0.56
Ω_{m}	$0.308^{+0.020}_{-0.024}$	0.300 ± 0.015	0.3051 ± 0.0075
σ_8	0.832 ± 0.017	0.813 ± 0.013	0.8361 ± 0.0092

The parameter values within our simpler G_{eff} one-parameter extension are given in Table VI. We note that for the MIν mode, the $\log_{10}(G_{\text{eff}}\text{MeV}^2)$ posterior is very non-Gaussian. As such, the 1σ error bar on G_{eff} (especially the lower bound), are only indicative. Table VII shows the $\Delta\chi^2$ between ΛCDM and its extension with $\Sigma m_\nu + N_{\text{eff}}$ and (the strong mode of) only G_{eff}. For both models the SIν mode prefers slightly

higher values of H_0 and σ_8 than the MIν mode given all the listed dataset combinations. Overall the estimated values of H_0 are lower than in ΛCDM due to its anticorrelation with neutrino mass, which is held fixed in ΛCDM.

APPENDIX B: MODE COMPARISON

In this appendix we supplement the comparison of the χ^2 values of SIν, MIν, and ΛCDM best-fit models with respect to different datasets and their components. Table VIII takes the SIν mode and MIν best fits to ACT, *Planck*, ACT + *WMAP*, and ACT + Planck datasets, and shows the difference in χ^2 between the two best fits for the components of the datasets. Table IX does the same with ACT + *WMAP* + BAO and ACT + Planck + BAO as the datasets. Table XI takes the MIν and ΛCDM best fits to ACT, *Planck*, ACT + *WMAP*, and ACT + Planck datasets, and shows the difference in χ^2 between the two best fits for the components of the datasets. Table X does the same with ACT + *WMAP* + BAO and ACT + Planck + BAO as the datasets for the SIν mode. Note that though MIν provides a better fit to the data than ΛCDM, it does not fit better than SIν.

TABLE VII. ACT + *WMAP* extension comparisons to ΛCDM ($\Delta\chi^2 = \chi^2_{\text{ext}} - \chi^2_{\Lambda\text{CDM}}$).

Parameter	$\sum m_\nu + N_{\text{eff}}$	G_{eff} SIν
$\Delta\chi^2_{\text{ACT}}$	-9.0	-12.1
$\Delta\chi^2_{\text{ACT:TT}}$	-1.4	-3.2
$\Delta\chi^2_{\text{ACT:TE}}$	-6.2	-2.8
$\Delta\chi^2_{\text{ACT:EE}}$	-1.4	-6.2
$\Delta\chi^2_{WMAP}$	0.5	-0.3
$\Delta\chi^2_{\text{CMB Total}}$	-8.6	-12.4
$\Delta\chi^2_{\text{prior}}$	0.1	0.3
$\Delta\chi^2_{\text{Total}}$	-8.4	-12.1
ΔAIC	-4.4	-10.1

TABLE VIII. Mode comparison. $\mathcal{B}_{\mathrm{SI}\nu}$ is the Bayes factor between the SIν and the MIν modes, $\mathcal{R}_{\mathrm{SI}\nu}$ is the maximum likelihood ratio, and $\Delta\chi^2 = \chi^2_{\mathrm{SI}\nu} - \chi^2_{\mathrm{MI}\nu}$.

Parameter	ACT	*Planck*	ACT + *WMAP*	ACT + *Planck*
$\mathcal{B}_{\mathrm{SI}\nu}$	1.5 ± 0.2	0.01 ± 0.01	2.8 ± 0.6	0.05 ± 0.02
$\mathcal{R}_{\mathrm{SI}\nu}$	2.6	0.4	6.5	1.1
$\Delta\chi^2_{\mathrm{ACT}}$	−1.9	⋯	−3.9	−1.6
$\Delta\chi^2_{\mathrm{ACT:TT}}$	−0.06	⋯	0.2	0.4
$\Delta\chi^2_{\mathrm{ACT:TE}}$	−0.6	⋯	0.4	−2.2
$\Delta\chi^2_{\mathrm{ACT:EE}}$	−1.3	⋯	−4.5	0.3
$\Delta\chi^2_{\mathrm{low}\ell}$	⋯	2.8	⋯	3.9
$\Delta\chi^2_{\mathrm{high}\ell}$	⋯	1.0	⋯	3.2
$\Delta\chi^2_{WMAP}$	⋯	⋯	0.1	⋯
$\Delta\chi^2_{\mathrm{CMB\ Total}}$	−1.9	3.8	−3.8	5.5
$\Delta\chi^2_{\mathrm{prior}}$	0.03	−2.0	8.6×10^{-3}	−5.7
$\Delta\chi^2_{\mathrm{Total}}$	−1.9	1.8	−3.7	−0.2

TABLE IX. Mode comparison for data combinations containing BAO measurements. $\mathcal{B}_{\mathrm{SI}\nu}$ is the Bayes factor between the SIν and the MIν modes, $\mathcal{R}_{\mathrm{SI}\nu}$ is the maximum likelihood ratio, and $\Delta\chi^2 = \chi^2_{\mathrm{SI}\nu} - \chi^2_{\mathrm{MI}\nu}$.

Parameter	ACT + *WMAP* + BAO	ACT + *Planck* + BAO
$\mathcal{B}_{\mathrm{SI}\nu}$	17.2 ± 4.7	0.1 ± 0.04
$\mathcal{R}_{\mathrm{SI}\nu}$	35.8	0.5
$\Delta\chi^2_{\mathrm{ACT}}$	−5.8	1.5
$\Delta\chi^2_{\mathrm{ACT:TT}}$	−0.5	−0.7
$\Delta\chi^2_{\mathrm{ACT:TE}}$	0.2	1.5
$\Delta\chi^2_{\mathrm{ACT:EE}}$	−5.5	0.8
$\Delta\chi^2_{\mathrm{low}\ell}$	⋯	3.8
$\Delta\chi^2_{\mathrm{high}\ell}$	⋯	−1.3
$\Delta\chi^2_{\mathrm{Lensing}}$	⋯	0.7
$\Delta\chi^2_{WMAP}$	−1.1	⋯
$\Delta\chi^2_{\mathrm{BAO}}$	−0.3	−0.7
$\Delta\chi^2_{\mathrm{CMB\ Total}}$	−6.9	4.7
$\Delta\chi^2_{\mathrm{prior}}$	0.07	−2.7
$\Delta\chi^2_{\mathrm{Total}}$	−7.2	1.3

TABLE X. Comparison to ΛCDM for the strongly interacting neutrino mode for data combinations containing BAO measurements ($\Delta\chi^2 = \chi^2_{\mathrm{SI}\nu} - \chi^2_{\Lambda\mathrm{CDM}}$).

Parameter	ACT + *WMAP* + BAO	ACT + *Planck* + BAO
$\Delta\chi^2_{\mathrm{ACT}}$	−13.0	−2.7
$\Delta\chi^2_{\mathrm{ACT:TT}}$	−2.9	−2.2
$\Delta\chi^2_{\mathrm{ACT:TE}}$	−4.1	−1.0
$\Delta\chi^2_{\mathrm{ACT:EE}}$	−6.0	0.5
$\Delta\chi^2_{\mathrm{low}\ell}$	⋯	5.6
$\Delta\chi^2_{\mathrm{high}\ell}$	⋯	−3.2

(Table continued)

TABLE X. *(Continued)*

Parameter	ACT + *WMAP* + BAO	ACT + *Planck* + BAO
$\Delta\chi^2_{\mathrm{Lensing}}$	⋯	0.4
$\Delta\chi^2_{WMAP}$	0.0	⋯
$\Delta\chi^2_{\mathrm{BAO}}$	−0.9	−0.3
$\Delta\chi^2_{\mathrm{CMB\ Total}}$	−13.0	0.1
$\Delta\chi^2_{\mathrm{prior}}$	0.7	−2.0
$\Delta\chi^2_{\mathrm{Total}}$	−13.2	−2.1
$\Delta\mathrm{AIC}$	−7.2	3.9

TABLE XI. Comparison to ΛCDM for the moderately interacting neutrino mode ($\Delta\chi^2 = \chi^2_{\mathrm{MI}\nu} - \chi^2_{\Lambda\mathrm{CDM}}$).

Parameter	ACT	*Planck*	ACT + *WMAP*	ACT + *Planck*
$\Delta\chi^2_{\mathrm{ACT}}$	−8.1	⋯	−11.0	−3.6
$\Delta\chi^2_{\mathrm{ACT:TT}}$	−2.7	⋯	−2.1	−1.5
$\Delta\chi^2_{\mathrm{ACT:TE}}$	0.6	⋯	−7.4	−2.1
$\Delta\chi^2_{\mathrm{ACT:EE}}$	−6.0	⋯	−1.5	−0.03
$\Delta\chi^2_{\mathrm{low}\ell}$	⋯	0.3	⋯	1.1
$\Delta\chi^2_{\mathrm{high}\ell}$	⋯	−0.6	⋯	−1.2
$\Delta\chi^2_{WMAP}$	⋯	⋯	0.7	⋯
$\Delta\chi^2_{\mathrm{CMB\ Total}}$	−8.1	−0.3	−10.3	−3.8
$\Delta\chi^2_{\mathrm{prior}}$	-7.5×10^{-4}	−1.1	0.4	2.3
$\Delta\chi^2_{\mathrm{Total}}$	−8.1	−1.4	−10.0	−1.5
$\Delta\mathrm{AIC}$	−2.1	4.6	−4.0	4.5

APPENDIX C: COMPLETE POSTERIOR PLOTS

We present the triangle plot showing $\log_{10}(G_{\text{eff}}\text{MeV}^2)$, N_{eff}, H_0, σ_8, $100\theta_*$, $10^9 A_s e^{-2\tau}$, n_s, and $\Omega_b h^2$ in Fig. 5. The posteriors were generated by varying the parameter spaces indicated in the legend with respect to ACT and *WMAP*.

Note the correlation between the value of $\log_{10}(G_{\text{eff}}\text{MeV}^2)$ in each island, and the values of $100\theta_*$, $10^9 A_s e^{-2\tau}$, and n_s, that is most clearly demonstrated by the red contours (ΛCDM augmented by $\log_{10}(G_{\text{eff}}\text{MeV}^2)$ only). This indicates that $\log_{10}(G_{\text{eff}}\text{MeV}^2)$ simultaneously impacts phase, amplitude, and tilt, respectively.
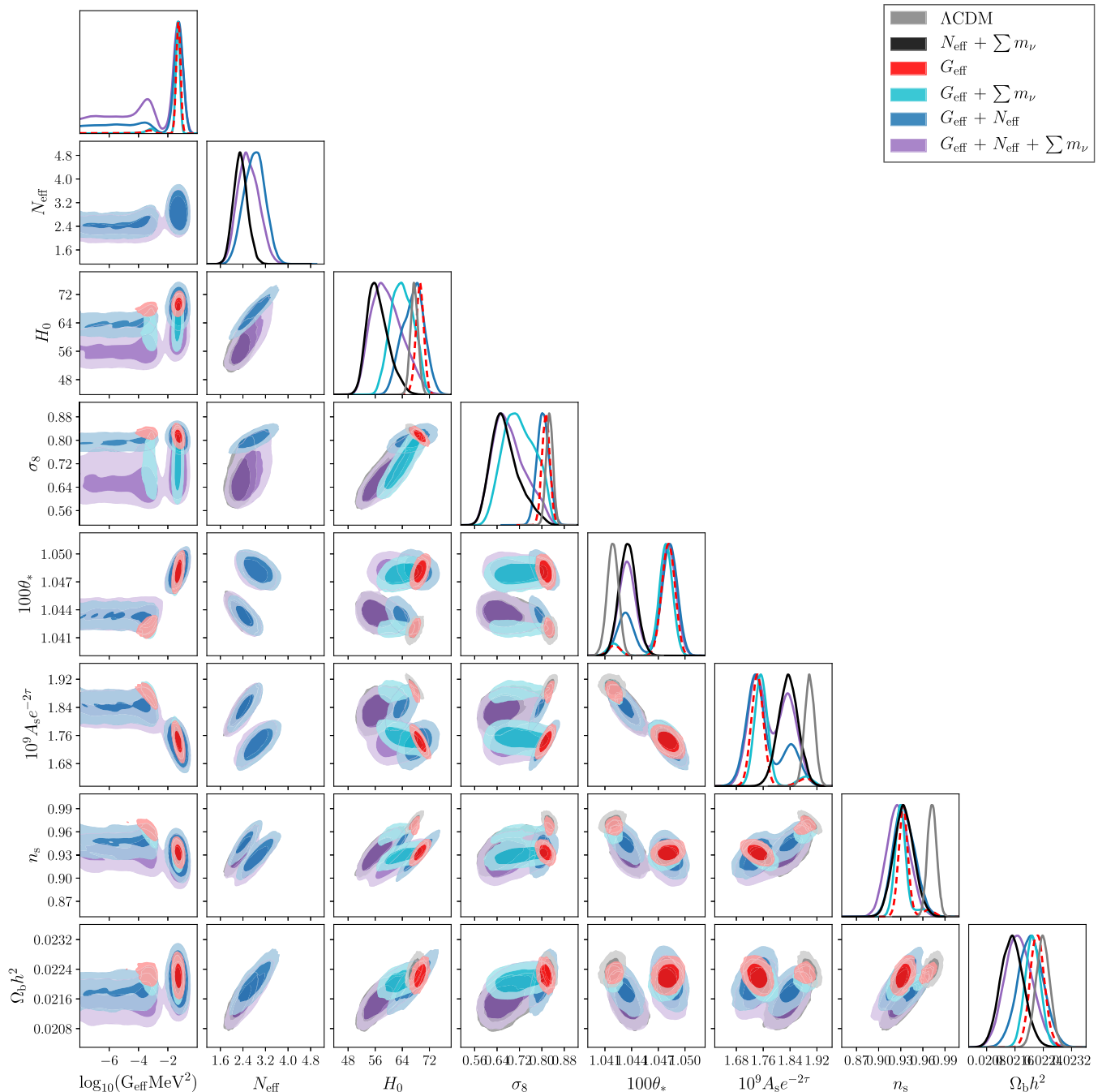
FIG. 5. Posterior distributions for $\log_{10}(G_{\text{eff}}\text{MeV}^2)$, N_{eff}, H_0, σ_8, $100\theta_*$, $10^9 A_s e^{-2\tau}$, n_s, and $\Omega_b h^2$ given ACT + *WMAP* data and various extensions of ΛCDM. The degeneracy between $\log_{10}(G_{\text{eff}}\text{MeV}^2)$ and $100\theta_*$, $10^9 A_s e^{-2\tau}$, and n_s (in the direction between the peaks of the two modes) indicates $\log_{10}(G_{\text{eff}}\text{MeV}^2)$'s ability to impact phase, amplitude, and tilt, simultaneously.

The G_{eff} model does not change the posteriors of H_0 and σ_8 significantly from the ΛCDM result but the other extensions do. The similarity of the $N_{\text{eff}} + \sum m_\nu$ contours and the baseline model contours indicate that the shift to lower H_0 is largely due to the variation in N_{eff} and $\sum m_\nu$. This is in contrast to the results of Ref. [96] where fitting the EDE model to ACT data resulted in a shift to higher values of H_0. Though the new physics introduced here and in Ref. [96] both appear compatible with ACT data and capture similar features, their relationships with the data are not identical.

APPENDIX D: CMB POWER SPECTRUM RESIDUALS

We present CMB power spectra from data and from theory predictions as residuals to the ΛCDM best fit predictions. Figure 6 shows the TT plots, Fig. 7 the TE plots, and Fig. 8 the EE plots. The left half of each figure shows ACT data points and theory predictions from best fits to datasets including ACT. The right half shows *Planck* data points and theory predictions from best fits to datasets including *Planck*. The top half of each figure shows SIν best fits, and the bottom half MIν best fits.
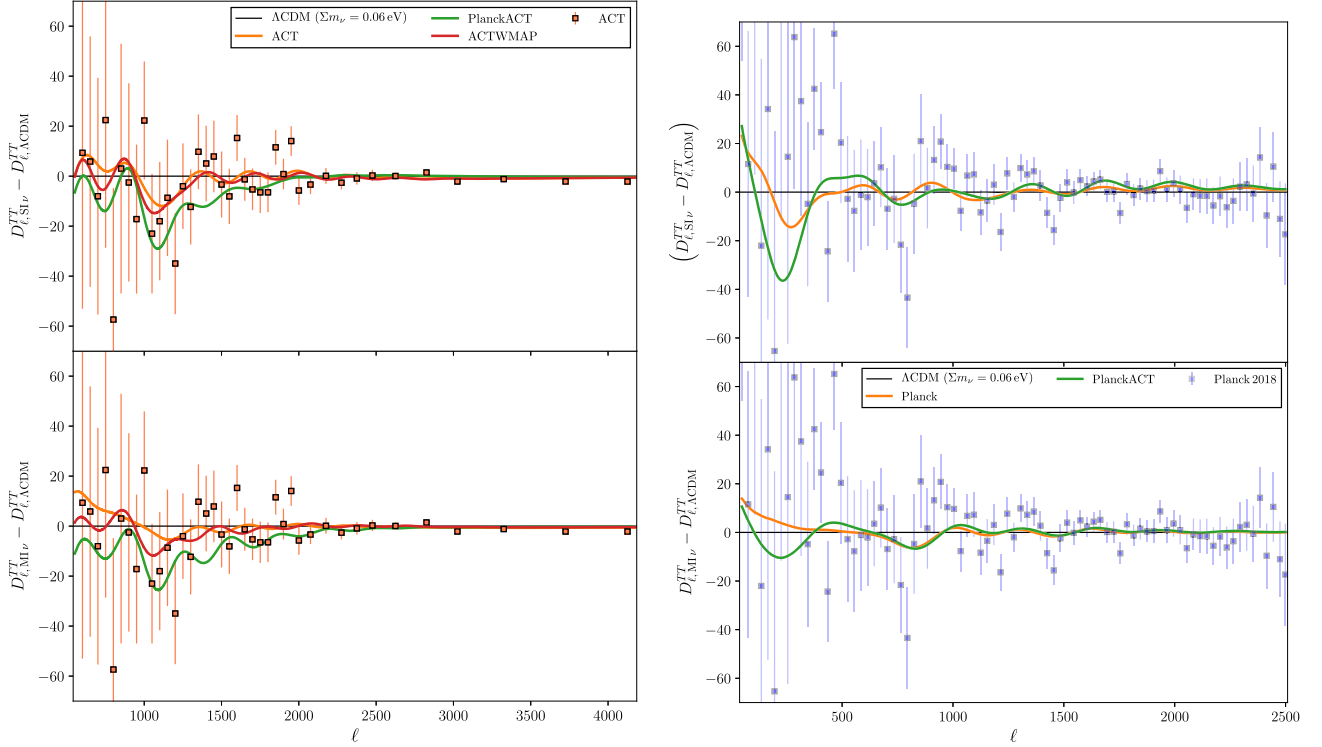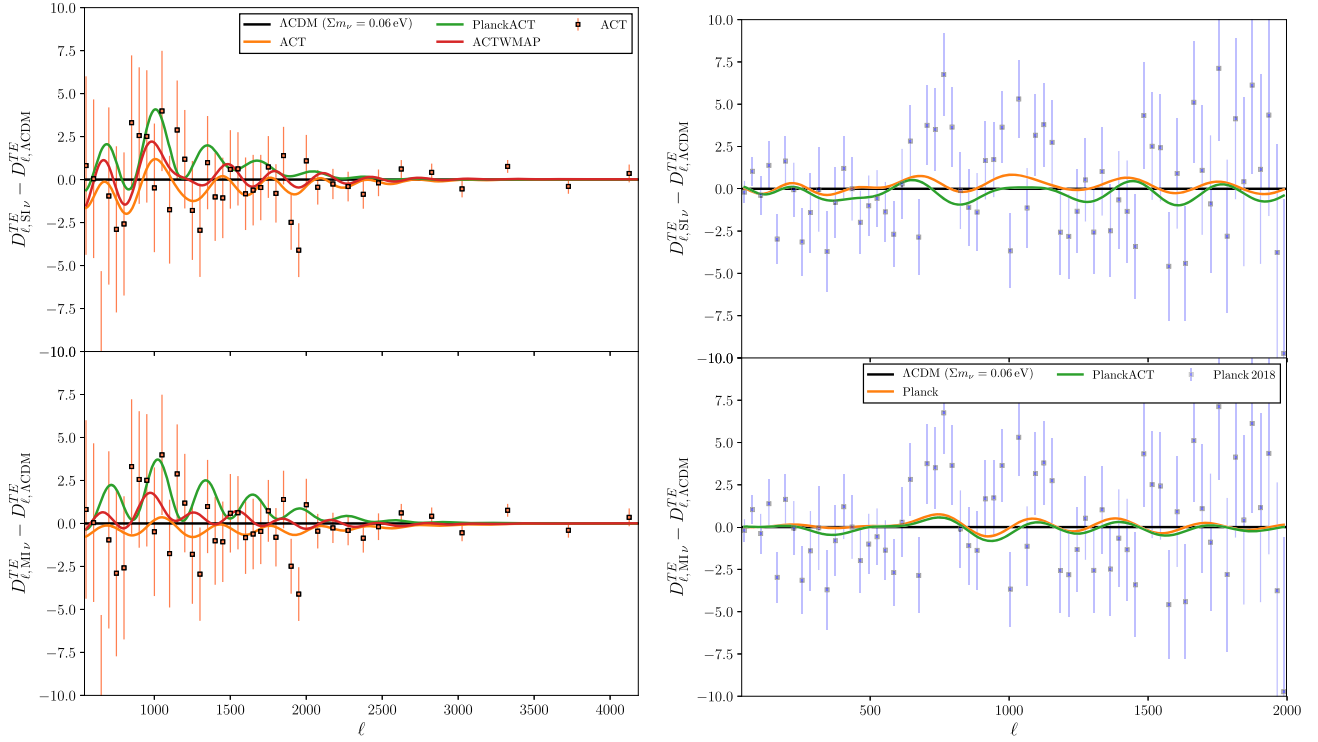

FIG. 6. Residuals of best-fit TT power spectra relative to ΛCDM (ACT best-fit ΛCDM for the left panel, *Planck* best-fit ΛCDM for the right panel). The upper panels are SIν best fits and the lower panels are MIν best fits.
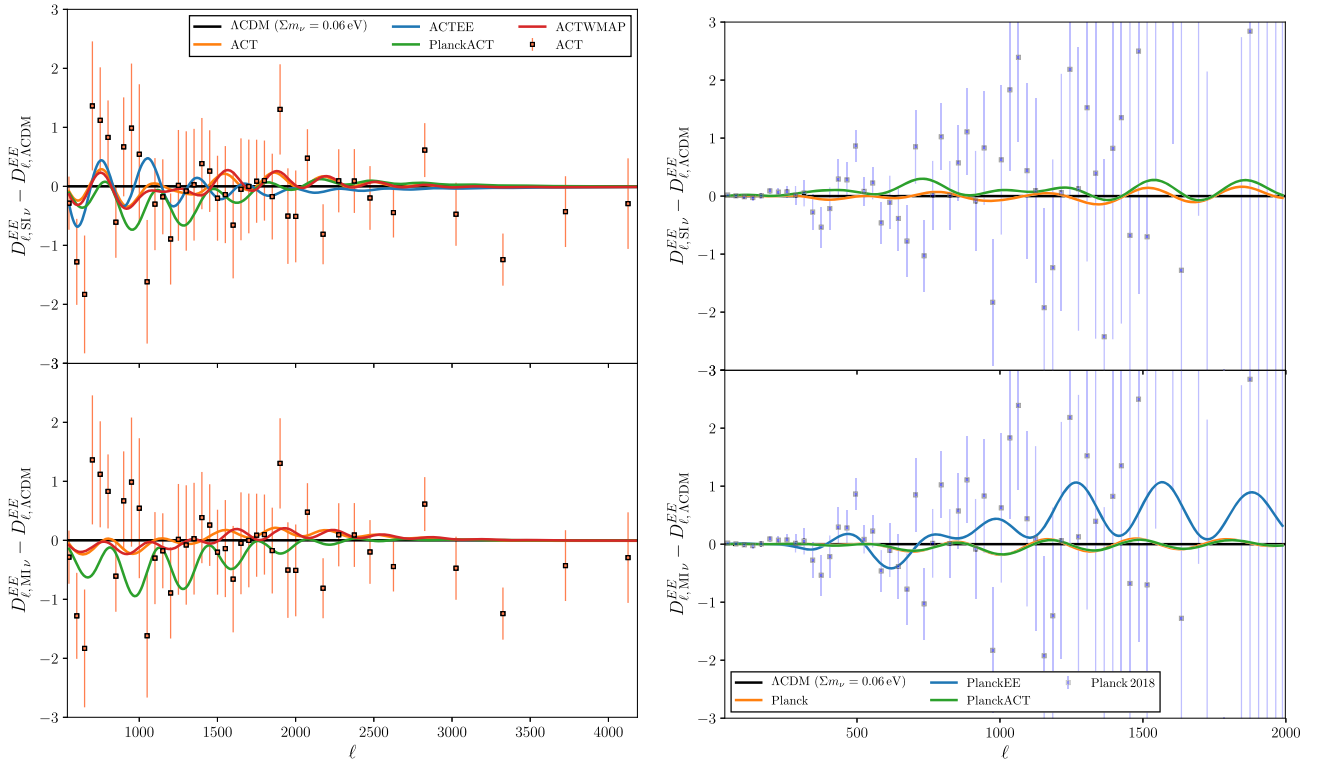
FIG. 7.	Residuals of best-fit TE power spectra relative to ΛCDM (ACT best-fit ΛCDM for the left panel, *Planck* best-fit ΛCDM for the right panel). The upper panels are SIν best fits and the lower panels are MIν best fits.

FIG. 8.	Residuals of best-fit EE power spectra relative to ΛCDM (ACT best-fit ΛCDM for the left panel, *Planck* best-fit ΛCDM for the right panel). The upper panels are SIν best fits and the lower panels are MIν best fits.

APPENDIX E: ADDING DISTANCE LADDER MEASUREMENTS

For completeness, we now discuss the addition of Cepheid calibrated distance-ladder Hubble constant measurements, $H_0 = 73.24 \pm 1.74$ km/s/Mpc measured by the SH_0ES team in 2016 [119], to our parameter constraints. Though there are more recent local measurements using Cepheid calibrated SNIa [120,121], TRGB calibrated SNIa [122,123], and strong lensing time delay [124], we utilize the SH_0ES team's 2016 measurements to directly

parallel the study done in [54]. Similar to when adding BAO measurements (see Sec. V), adding the SH_0ES H_0 measurements decreases the significance of the MIν mode and decreases the width of the SIν mode (compare ACT + $WMAP$ + BAO + SH_0ES to ACT + $WMAP$ + BAO in Fig. 9). Adding in distance ladder H_0 measurements from SH_0ES nearly eliminates the MIν mode as a viable statistical possibility. That is, SIν is the mode more compatible with the combination of ACT + $WMAP$ + BAO + SH_0ES than MIν.
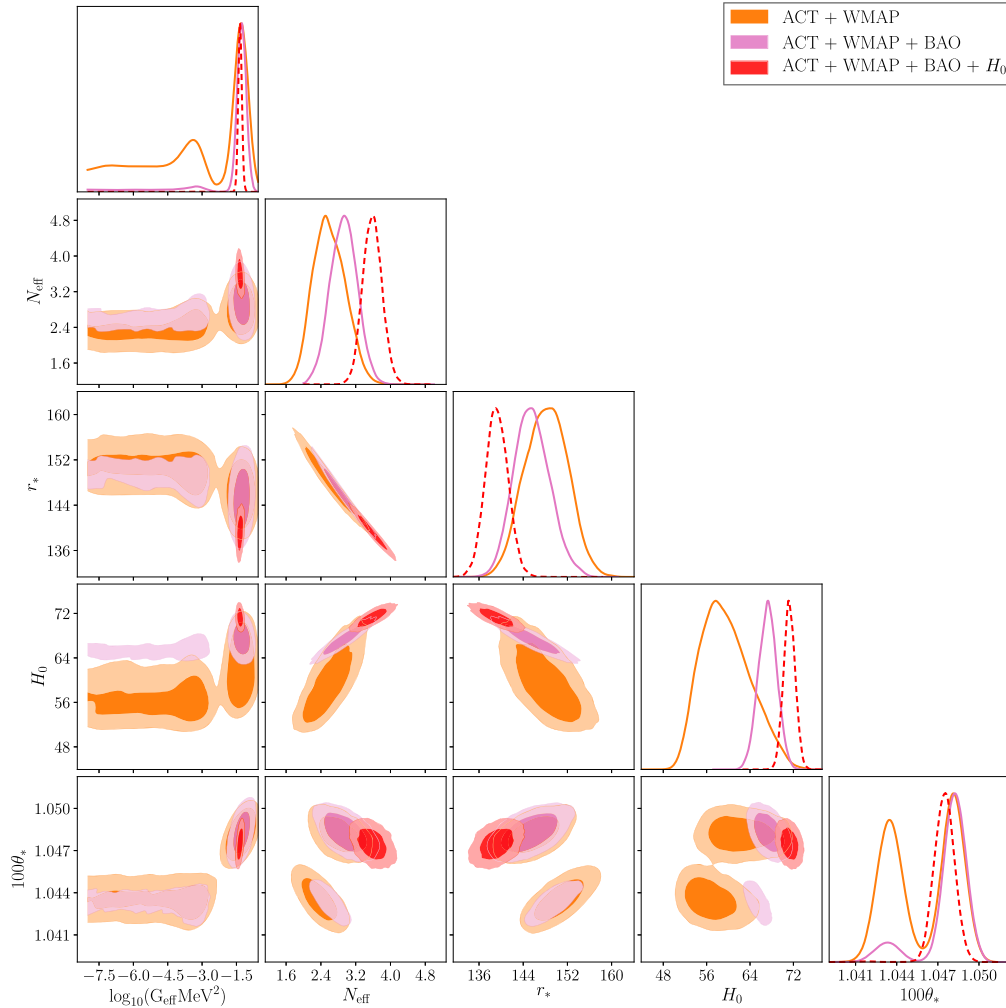

FIG. 9. Posteriors for $\log_{10}(G_{\mathrm{eff}}\mathrm{MeV}^2)$, N_{eff}, r_* (the comoving size of sound horizon at recombination), H_0, and $100\theta_*$ (the angular size of sound horizon at last scattering) with ACT + $WMAP$ (orange), ACT + $WMAP$ + BAO (pink), and ACT + $WMAP$ + BAO + SH_0ES (red) dataset combinations. The introduction of distance ladder measurements on top of BAO measurements, which already suppresses the MIν mode, nearly removes the MIν mode.
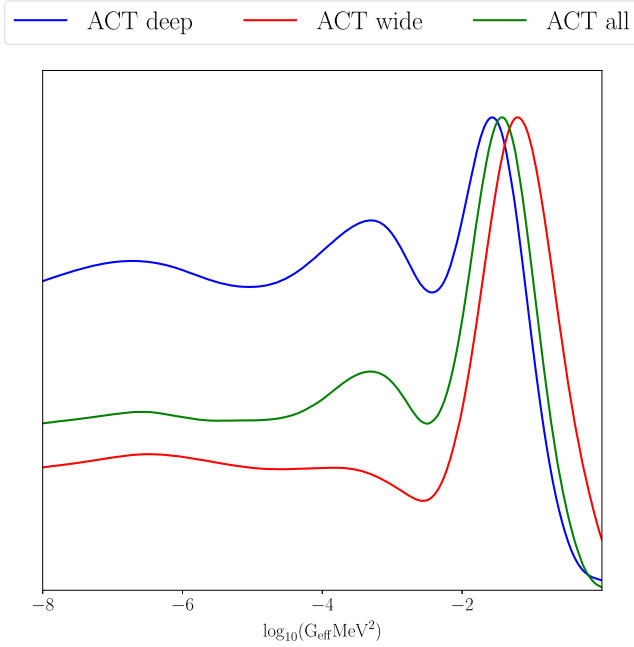
FIG. 10. 1D posterior for $G_{\rm eff}$, obtained by varying the 6 ΛCDM parameters, Σm_ν, $N_{\rm eff}$, and $G_{\rm eff}$ with all of ACT (in green), "deep" ACT (in blue), and "wide" ACT (in red). The "wide" only posterior shows the strongest preference for SIν but the blue posterior also does slightly prefer SIν.

APPENDIX F: ACT WIDE/DEEP

Fig. 10 shows the 1D posterior of $\log_{10}(G_{\rm eff}{\rm MeV}^2)$ for ACT "deep," ACT "wide," and the full ACT dataset. We find that both the posteriors produced with "deep" and "wide" have a preference for $\log_{10}(G_{\rm eff}{\rm MeV}^2) \sim -1.3$ around which their tallest peaks and best-fit models are located. However, the preference for SIν over MIν is much

TABLE XII. ACT deep and wide comparisons to ΛCDM ($\Delta\chi^2 = \chi^2_{\rm SI\nu} - \chi^2_{\Lambda{\rm CDM}}$).

Parameter	ACT deep	ACT wide
$\Delta\chi^2_{\rm ACT}$	−4.4	−8.0
$\Delta\chi^2_{\rm ACT:TT}$	−5.0	0.8
$\Delta\chi^2_{\rm ACT:TE}$	0.3	1.4
$\Delta\chi^2_{\rm ACT:EE}$	0.3	−10.1
$\Delta\chi^2_{\rm prior}$	0.01	0.01
$\Delta\chi^2_{\rm Total}$	−4.4	−7.9
ΔAIC	1.6	−1.9

stronger with "wide" than with "deep," resulting in the combined ACT posterior which is between the two other posteriors. We show $\Delta\chi^2$ values comparing SIν to ΛCDM for the isolated "deep" and "wide" components of ACT in Table XII. The "wide" E-mode polarization is the only component with a strong enough preference for SIν to bring ΔAIC < 0 compared to ΛCDM.

We show the "wide" and "deep" E-mode polarization residuals in Fig. 11. While the "wide" data show a stronger fluctuation in $700 \lesssim \ell \lesssim 1000$, the large error bars of the "deep" data are still consistent with this fluctuation. Therefore, the discrepancies between the preferences of "wide" and "deep" are within the margins of error of the two components of ACT.

This is again similar to the findings in Ref. [96] that the feature which the EDE model fits better than ΛCDM is more pronounced in the "wide" component (specifically "wide" EE) than the "deep," further suggesting that the two different physical models maybe describing the same feature in ACT data.
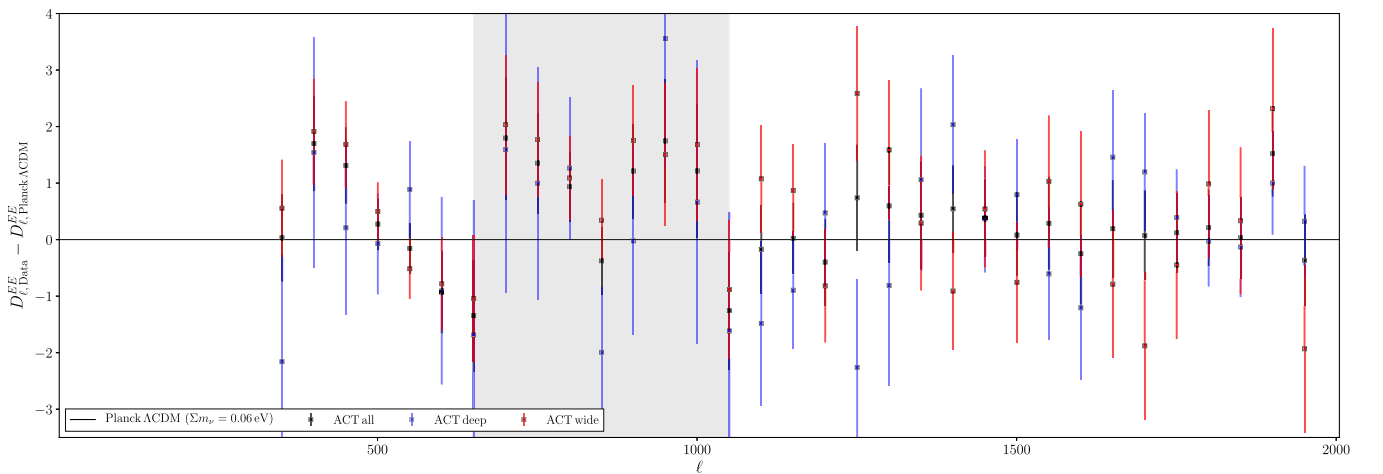

FIG. 11. Difference for the E-mode polarization data for ACT wide, deep, and total compared to the best-fit ΛCDM model from *Planck*. In the $700 \lesssim \ell \lesssim 1000$ range of interest, the three datasets are not significantly far apart.
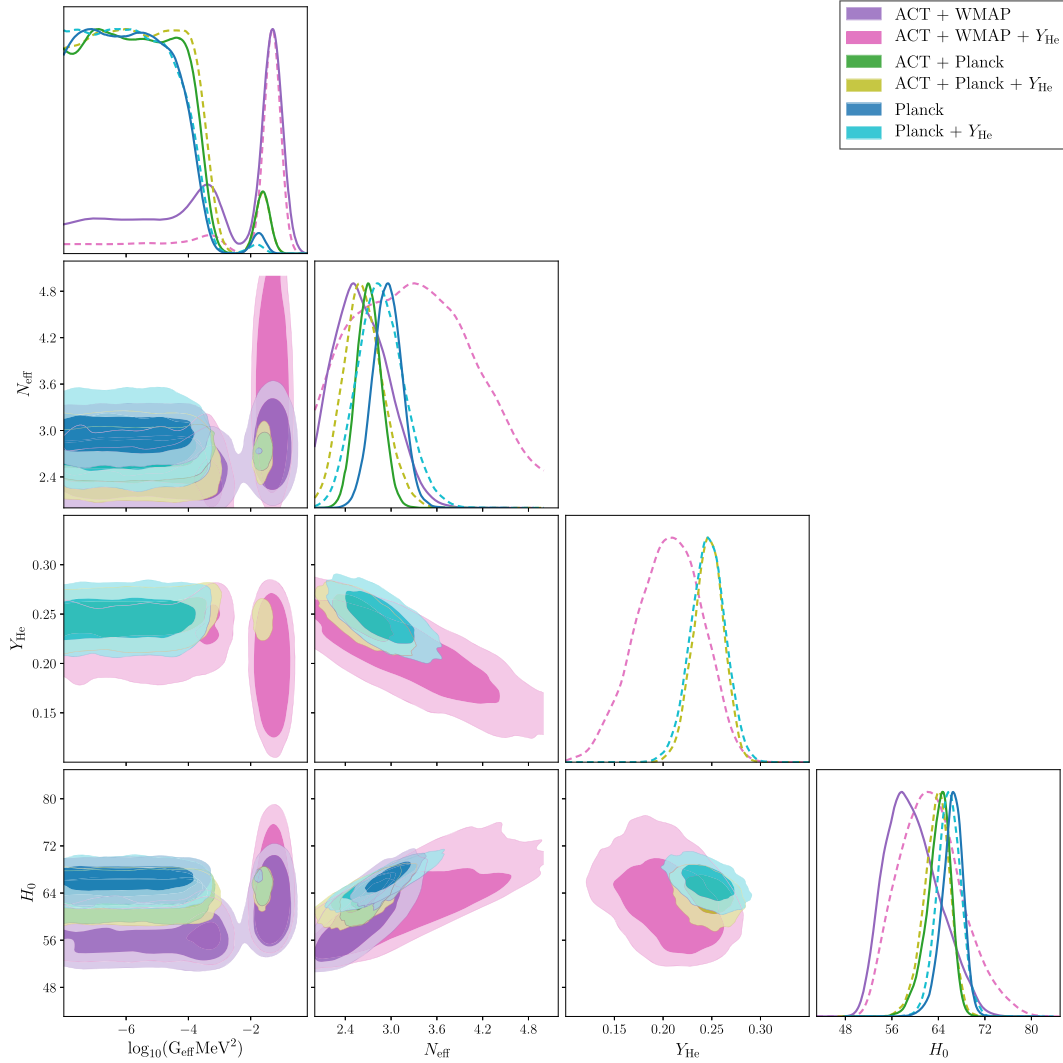
FIG. 12. Posteriors for $\log_{10}(G_{\text{eff}}\text{MeV}^2)$, N_{eff}, Y_{He}, and H_0 for various CMB dataset combinations. Notice how letting Y_{He} vary decreases the significance of MIν with ACT + *WMAP*, but when *Planck* is involved, there is hardly any change as *Planck* is able to constrain Y_{He} without BBN inputs.

APPENDIX G: HELIUM ABUNDANCE

In this section, we consider the impact of freeing the helium abundance Y_{He} away from its big bang nucleosynthesis (BBN) value. We now thus consider a four-parameter extension of ΛCDM in which G_{eff}, N_{eff}, $\sum m_\nu$, and Y_{He} are allowed to vary freely. Our results are summarized in Fig. 12 for different data set combinations. For ACT + *WMAP*, freeing the helium fraction boosts the SIν mode, largely due to the large range of N_{eff} and Y_{He} values that are now accessible within this mode of the posterior. In the Standard Model, BBN predicts a larger helium yield Y_{He} as N_{eff} is increased. However, maintaining the ratio of the photon scattering rate to the Hubble rate constant near recombination, which is necessary to leave the CMB invariant [91], requires Y_{He} to *decrease* as N_{eff} is increased. This can be seen in the strong anticorrelation between N_{eff} and Y_{He} in Fig. 12 for the ACT + *WMAP* + Y_{He} case. Since the MIν mode is constrained to have low values of N_{eff} as explained above, only the SIν mode can exploit this degeneracy once the helium abundance is allowed to vary freely.

On the other hand, freeing Y_{He} in the presence of *Planck* data has little impact on the posterior, illustrating the ability of *Planck* data to constrain the helium abundance even without BBN inputs. Just as in our baseline model, the *Planck* data strongly disfavor the SIν mode compared to the MIν mode.

[1] N. Aghanim *et al.* (Planck Collaboration), Astron. Astrophys. **641**, A6 (2020); **652**, C4(E) (2021).

[2] M. Lattanzi and M. Gerbino, Front. Phys. **5**, 70 (2018).

[3] A. A. Aguilar-Arevalo *et al.* (MiniBooNE Collaboration), Phys. Rev. Lett. **121**, 221801 (2018).

[4] A. Aguilar-Arevalo *et al.* (LSND Collaboration), Phys. Rev. D **64**, 112007 (2001).

[5] M. G. Aartsen *et al.* (IceCube Collaboration), Phys. Rev. D **95**, 112002 (2017).

[6] M. G. Aartsen *et al.* (IceCube Collaboration), Phys. Rev. Lett. **117**, 071801 (2016).

[7] P. Adamson *et al.* (NOvA Collaboration), Phys. Rev. D **96**, 072006 (2017).

[8] P. Adamson *et al.* (MINOS + Collaboration), Phys. Rev. Lett. **122**, 091803 (2019).

[9] M. Dentler, Á. Hernández-Cabezudo, J. Kopp, P. A. N. Machado, M. Maltoni, I. Martinez-Soler, and T. Schwetz, J. High Energy Phys. 08 (2018) 010.

[10] G. Choi, C.-T. Chiang, and M. LoVerde, J. Cosmol. Astropart. Phys. 06 (2018) 044.

[11] N. Song, M. C. Gonzalez-Garcia, and J. Salvado, J. Cosmol. Astropart. Phys. 10 (2018) 055.

[12] C. S. Lorenz, L. Funcke, E. Calabrese, and S. Hannestad, Phys. Rev. D **99**, 023501 (2019).

[13] G. Barenboim, P. B. Denton, and I. M. Oldengott, Phys. Rev. D **99**, 083515 (2019).

[14] F. Forastieri, M. Lattanzi, and P. Natoli, Phys. Rev. D **100**, 103526 (2019).

[15] A. Y. Smirnov and X.-J. Xu, J. High Energy Phys. 12 (2019) 046.

[16] M. Escudero and S. J. Witte, Eur. Phys. J. C **80**, 294 (2020).

[17] S. Ghosh, R. Khatri, and T. S. Roy, Phys. Rev. D **102**, 123544 (2020).

[18] L. Funcke, G. Raffelt, and E. Vitagliano, Phys. Rev. D **101**, 015025 (2020).

[19] J. Sakstein and M. Trodden, Phys. Rev. Lett. **124**, 161301 (2020).

[20] A. Mazumdar, S. Mohanty, and P. Parashari, Phys. Rev. D **101**, 083521 (2020).

[21] N. Blinov and G. Marques-Tavares, J. Cosmol. Astropart. Phys. 09 (2020) 029.

[22] A. de Gouvêa, P. S. B. Dev, B. Dutta, T. Ghosh, T. Han, and Y. Zhang, J. High Energy Phys. 07 (2020) 142.

[23] J. Froustey, C. Pitrou, and M. C. Volpe, J. Cosmol. Astropart. Phys. 12 (2020) 015.

[24] K. S. Babu, G. Chauhan, and P. S. Bhupal Dev, Phys. Rev. D **101**, 095029 (2020).

[25] F. F. Deppisch, L. Graf, W. Rodejohann, and X.-J. Xu, Phys. Rev. D **102**, 051701 (2020).

[26] K. J. Kelly, M. Sen, W. Tangarife, and Y. Zhang, Phys. Rev. D **101**, 115031 (2020).

[27] M. Escudero Abenza, J. Cosmol. Astropart. Phys. 05 (2020) 048.

[28] H.-J. He, Y.-Z. Ma, and J. Zheng, J. Cosmol. Astropart. Phys. 11 (2020) 003.

[29] G.-J. Ding and F. Feruglio, J. High Energy Phys. 06 (2020) 134.

[30] M. Berbig, S. Jana, and A. Trautner, Phys. Rev. D **102**, 115008 (2020).

[31] A. Gogoi, R. K. Sharma, P. Chanda, and S. Das, Astrophys. J. **915**, 132 (2021).

[32] G. Barenboim and U. Nierste, Phys. Rev. D **104**, 023013 (2021).

[33] A. Das and S. Ghosh, J. Cosmol. Astropart. Phys. 07 (2021) 038.

[34] A. Mazumdar, S. Mohanty, and P. Parashari, J. Cosmol. Astropart. Phys. 10 (2022) 011.

[35] T. Brinckmann, J. H. Chang, and M. LoVerde, Phys. Rev. D **104**, 063523 (2021).

[36] K. J. Kelly, M. Sen, and Y. Zhang, Phys. Rev. Lett. **127**, 041101 (2021).

[37] I. Esteban and J. Salvado, J. Cosmol. Astropart. Phys. 05 (2021) 036.

[38] F. Arias-Aragon, E. Fernandez-Martinez, M. Gonzalez-Lopez, and L. Merlo, Eur. Phys. J. C **81**, 28 (2021).

[39] Y. Du and J.-H. Yu, J. High Energy Phys. 05 (2021) 058.

[40] M. Carrillo González, Q. Liang, J. Sakstein, and M. Trodden, J. Cosmol. Astropart. Phys. 04 (2021) 063.

[41] G.-y. Huang and W. Rodejohann, Phys. Rev. D **103**, 123007 (2021).

[42] A. Sung, G. Guo, and M.-R. Wu, Phys. Rev. D **103**, 103005 (2021).

[43] M. Escudero and S. J. Witte, Eur. Phys. J. C **81**, 515 (2021).

[44] S. Roy Choudhury, S. Hannestad, and T. Tram, J. Cosmol. Astropart. Phys. 03 (2021) 084.

[45] J. A. Carpio, K. Murase, I. M. Shoemaker, and Z. Tabrizi, Phys. Rev. D **107**, 103057 (2023).

[46] N. Orlofsky and Y. Zhang, Phys. Rev. D **104**, 075010 (2021).

[47] I. Esteban, S. Pandey, V. Brdar, and J. F. Beacom, Phys. Rev. D **104**, 123014 (2021).

[48] J. Venzor, G. Garcia-Arroyo, A. Pérez-Lorenzana, and J. De-Santiago, Phys. Rev. D **105**, 123539 (2022).

[49] S. Bashinsky and U. Seljak, Phys. Rev. D **69**, 083002 (2004).

[50] Z. Hou, R. Keisler, L. Knox, M. Millea, and C. Reichardt, Phys. Rev. D **87**, 083008 (2013).

[51] B. Follin, L. Knox, M. Millea, and Z. Pan, Phys. Rev. Lett. **115**, 091301 (2015).

[52] F.-Y. Cyr-Racine and K. Sigurdson, Phys. Rev. D **90**, 123533 (2014).

[53] D. Baumann, D. Green, J. Meyers, and B. Wallisch, J. Cosmol. Astropart. Phys. 01 (2016) 007.

[54] C. D. Kreisch, F.-Y. Cyr-Racine, and O. Doré, Phys. Rev. D **101**, 123505 (2020).

[55] M. Archidiacono and S. Hannestad, J. Cosmol. Astropart. Phys. 07 (2014) 046.

[56] L. Lancaster, F.-Y. Cyr-Racine, L. Knox, and Z. Pan, J. Cosmol. Astropart. Phys. 07 (2017) 033.

[57] I. M. Oldengott, T. Tram, C. Rampf, and Y. Y. Y. Wong, J. Cosmol. Astropart. Phys. 11 (2017) 027.

[58] M. Park, C. D. Kreisch, J. Dunkley, B. Hadzhiyska, and F.-Y. Cyr-Racine, Phys. Rev. D **100**, 063524 (2019).

[59] K. C. Y. Ng and J. F. Beacom, Phys. Rev. D **90**, 065035 (2014).

[60] E. Grohs, G. M. Fuller, and M. Sen, J. Cosmol. Astropart. Phys. 07 (2020) 001.

[61] E. W. Kolb and M. S. Turner, Phys. Rev. D **36**, 2895 (1987).

[62] A. Manohar, Phys. Lett. B **192**, 217 (1987).

[63] D. A. Dicus, S. Nussinov, P. B. Pal, and V. L. Teplitz, Phys. Lett. B **218**, 84 (1989).

[64] H. Davoudiasl and P. Huber, Phys. Rev. Lett. **95**, 191302 (2005).

[65] M. Sher and C. Triola, Phys. Rev. D **83**, 117702 (2011).

[66] P. Fayet, D. Hooper, and G. Sigl, Phys. Rev. Lett. **96**, 211302 (2006).

[67] K. Choi and A. Santamaria, Phys. Rev. D **42**, 293 (1990).

[68] M. Blennow, A. Mirizzi, and P. D. Serpico, Phys. Rev. D **78**, 113004 (2008).

[69] S. Galais, J. Kneller, and C. Volpe, J. Phys. G **39**, 035201 (2012).

[70] M. Kachelriess, R. Tomas, and J. Valle, Phys. Rev. D **62**, 023004 (2000).

[71] Y. Farzan, Phys. Rev. D **67**, 073015 (2003).

[72] S. Zhou, Phys. Rev. D **84**, 038701 (2011).

[73] Y. S. Jeong, S. Palomares-Ruiz, M. H. Reno, and I. Sarcevic, J. Cosmol. Astropart. Phys. 06 (2018) 019.

[74] P.-W. Chang, I. Esteban, J. F. Beacom, T. A. Thompson, and C. M. Hirata, Phys. Rev. Lett. **131**, 071002 (2023).

[75] B. Ahlgren, T. Ohlsson, and S. Zhou, Phys. Rev. Lett. **111**, 199001 (2013).

[76] G.-y. Huang, T. Ohlsson, and S. Zhou, Phys. Rev. D **97**, 075009 (2018).

[77] J. Venzor, A. Pérez-Lorenzana, and J. De-Santiago, Phys. Rev. D **103**, 043534 (2021).

[78] K. Ioka and K. Murase, Prog. Theor. Exp. Phys. **2014**, 061E01 (2014).

[79] J. F. Cherry, A. Friedland, and I. M. Shoemaker, arXiv:1605.06506.

[80] M. S. Bilenky, S. M. Bilenky, and A. Santamaria, Phys. Lett. B **301**, 287 (1993).

[81] D. Y. Bardin, S. M. Bilenky, and B. Pontecorvo, Phys. Lett. **32B**, 121 (1970).

[82] M. S. Bilenky and A. Santamaria, arXiv:hep-ph/9908272.

[83] V. Brdar, M. Lindner, S. Vogl, and X.-J. Xu, Phys. Rev. D **101**, 115001 (2020).

[84] K.-F. Lyu, E. Stamou, and L.-T. Wang, Phys. Rev. D **103**, 015004 (2021).

[85] A. P. Lessa and O. L. G. Peres, Phys. Rev. D **75**, 094001 (2007).

[86] P. Bakhti and Y. Farzan, Phys. Rev. D **95**, 095008 (2017).

[87] G. Arcadi, J. Heeck, F. Heizmann, S. Mertens, F. S. Queiroz, W. Rodejohann, M. Slezák, and K. Valerius, J. High Energy Phys. 01 (2019) 206.

[88] N. Blinov, K. J. Kelly, G. Z. Krnjaic, and S. D. McDermott, Phys. Rev. Lett. **123**, 191102 (2019).

[89] L. Verde, T. Treu, and A. G. Riess, Nat. Astron. **3**, 891 (2019).

[90] E. Di Valentino, O. Mena, S. Pan, L. Visinelli, W. Yang, A. Melchiorri, D. F. Mota, A. G. Riess, and J. Silk, Classical Quantum Gravity **38**, 153001 (2021).

[91] F.-Y. Cyr-Racine, F. Ge, and L. Knox, Phys. Rev. Lett. **128**, 201301 (2022).

[92] D. Baumann, D. Green, and M. Zaldarriaga, J. Cosmol. Astropart. Phys. 11 (2017) 007.

[93] S. Aiola, E. Calabrese, L. Maurin, S. Naess, B. L. Schmitt, M. H. Abitbol, G. E. Addison, P. A. Ade, D. Alonso, M. Amiri *et al.*, J. Cosmol. Astropart. Phys. 12 (2020) 047.

[94] P. Ade *et al.* (Simons Observatory Collaboration), J. Cosmol. Astropart. Phys. 02 (2019) 056.

[95] K. N. Abazajian, P. Adshead, Z. Ahmed, S. W. Allen, D. Alonso, K. S. Arnold, C. Baccigalupi, J. G. Bartlett, N. Battaglia, B. A. Benson *et al.*, arXiv:1610.02743.

[96] J. C. Hill, E. Calabrese, S. Aiola, N. Battaglia, B. Bolliet, S. K. Choi, M. J. Devlin, A. J. Duivenvoorden, J. Dunkley, S. Ferraro *et al.*, Phys. Rev. D **105**, 123536 (2022).

[97] M. A. Corona, R. Murgia, M. Cadeddu, M. Archidiacono, S. Gariazzo, C. Giunti, and S. Hannestad, J. Cosmol. Astropart. Phys. 06 (2022) 010.

[98] G. Hinshaw *et al.* (WMAP Collaboration), Astrophys. J. Suppl. Ser. **208**, 19 (2013).

[99] C. L. Bennett *et al.* (WMAP Collaboration), Astrophys. J. Suppl. Ser. **208**, 20 (2013).

[100] I. M. Oldengott, C. Rampf, and Y. Y. Y. Wong, J. Cosmol. Astropart. Phys. 04 (2015) 016.

[101] A. Lewis, A. Challinor, and A. Lasenby, Astrophys. J. **538**, 473 (2000).

[102] A. Lewis and S. Bridle, Phys. Rev. D **66**, 103511 (2002).

[103] F. Feroz and M. P. Hobson, Mon. Not. R. Astron. Soc. **384**, 449 (2008).

[104] J. Skilling, Bayesian Anal. **1**, 833 (2006).

[105] S. K. Choi, M. Hasselfield, S.-P. P. Ho, B. Koopman, M. Lungu, M. H. Abitbol, G. E. Addison, P. A. Ade, S. Aiola, D. Alonso *et al.*, J. Cosmol. Astropart. Phys. 12 (2020) 045.

[106] N. Aghanim *et al.* (Planck Collaboration), Astron. Astrophys. **641**, A5 (2020).

[107] F. Beutler, C. Blake, M. Colless, D. H. Jones, L. Staveley-Smith, L. Campbell, Q. Parker, W. Saunders, and F. Watson, Mon. Not. R. Astron. Soc. **416**, 3017 (2011).

[108] F. D. Albareti, C. Allende Prieto, A. Almeida, F. Anders, S. Anderson, B. H. Andrews, A. Aragón-Salamanca, M. Argudo-Fernández, E. Armengaud, E. Aubourg *et al.*, Astrophys. J. Suppl. Ser. **233**, 25 (2017).

[109] A. J. Ross, L. Samushia, C. Howlett, W. J. Percival, A. Burden, and M. Manera, Mon. Not. R. Astron. Soc. **449**, 835 (2015).

[110] N. Aghanim *et al.* (Planck Collaboration), Astron. Astrophys. **641**, A8 (2020).

[111] H. Akaike, IEEE Trans. Autom. Control **19**, 716 (1974).

[112] A. F. Jarosz and J. Wiley, J. Prob. Solving **7** (2014).

[113] Y. Akrami, M. Ashdown, J. Aumont, C. Baccigalupi, M. Ballardini, A. J. Banday, R. B. Barreiro, N. Bartolo, S. Basak *et al.* (Planck Collaboration), Astron. Astrophys. **641**, A4 (2020).

[114] A. Friedland, K. M. Zurek, and S. Bashinsky, arXiv:0704.3271.

[115] D. Dutcher *et al.* (SPT-3G Collaboration), Phys. Rev. D **104**, 022003 (2021).

[116] J. D. Hunter, Comput. Sci. Eng. **9**, 90 (2007).

[117] C. R. Harris, K. J. Millman, S. J. van der Walt, R. Gommers, P. Virtanen, D. Cournapeau, E. Wieser, J. Taylor, S. Berg, N. J. Smith *et al.*, Nature (London) **585**, 357 (2020).

[118] A. Lewis, arXiv:1910.13970.

[119] A. G. Riess, L. M. Macri, S. L. Hoffmann, D. Scolnic, S. Casertano, A. V. Filippenko, B. E. Tucker, M. J. Reid, D. O. Jones, J. M. Silverman *et al.*, Astrophys. J. **826**, 56 (2016).

[120] A. G. Riess, S. Casertano, W. Yuan, J. B. Bowers, L. Macri, J. C. Zinn, and D. Scolnic, Astrophys. J. Lett. **908**, L6 (2021).

[121] A. G. Riess *et al.*, Astrophys. J. Lett. **934**, L7 (2022).

[122] W. L. Freedman, B. F. Madore, T. Hoyt, I. S. Jang, R. Beaton, M. G. Lee, A. Monson, J. Neeley, and J. Rich, Astrophys. J. **891**, 57 (2020).

[123] W. L. Freedman, Astrophys. J. **919**, 16 (2021).

[124] S. Birrer *et al.*, Astron. Astrophys. **643**, A165 (2020).